A-SITE ENGINEERED DOUBLE PEROVSKITE OXIDE AS AIR ELECTRODE FOR RECHARGEABLE Zn-AIR BATTERIES

A THESIS SUBMITTED TO
THE GRADUATE SCHOOL OF NATURAL AND APPLIED SCIENCES
OF
MIDDLE EAST TECHNICAL UNIVERSITY

BY

TUNCAY ERDİL

IN PARTIAL FULFILLMENT OF THE REQUIREMENTS
FOR
THE DEGREE OF MASTER OF SCIENCE
IN
METALLURGICAL AND MATERIALS ENGINEERING

SEPTEMBER 2023

Approval of the thesis:

A-SITE ENGINEERED DOUBLE PEROVSKITE OXIDE AS AIR ELECTRODE FOR RECHARGEABLE Zn-AIR BATTERIES

submitted by **TUNCAY ERDİL** in partial fulfillment of the requirements for the degree of **Master of Science** i**n Metallurgical and Materials Engineering, Middle East Technical University** by,

Prof. Dr. Halil Kalıpçılar
Dean, Graduate School of **Natural and Applied Sciences** _____

Prof. Dr. Ali Kalkanlı
Head of the Department, **Met. and Mat. Eng.** _____

Assist. Prof. Dr. Çiğdem Toparlı
Supervisor, **Met. and Mat. Eng., METU** _____

Examining Committee Members:

Prof. Dr. Kadri Aydınol
Metallurgical and Materials Eng, METU _____

Assist. Prof. Dr. Çiğdem Toparlı
Metallurgical and Materials Eng, METU _____

Prof. Dr. Yunus Eren Kalay
Metallurgical and Materials Eng, METU _____

Assist. Prof. Dr. Necip Berker Üner
Chemical Eng, METU _____

Assoc. Prof. Dr. Burak Ülgüt
Chemistry, Bilkent Uni. _____

Date: 06.09.2023

I hereby declare that all information in this document has been obtained and presented in accordance with academic rules and ethical conduct. I also declare that, as required by these rules and conduct, I have fully cited and referenced all material and results that are not original to this work.

Name Last name : Tuncay Erdil

Signature :

ABSTRACT

A-SITE ENGINEERED DOUBLE PEROVSKITE OXIDE AS AIR ELECTRODE FOR RECHARGEABLE Zn-AIR BATTERIES

Erdil, Tuncay
Master of Science, Metallurgical and Materials Engineering
Supervisor: Assist. Prof. Dr. Çiğdem Toparlı

September 2023, 88 pages

Electrochemical energy storage and conversion devices, such as rechargeable metal-air batteries, water electrolyzers, and fuel cells, heavily rely on the electrochemical oxygen evolution reaction (OER) and oxygen reduction reaction (ORR). The OER, characterized by slow reaction kinetics, poses challenges to the efficiency of these devices. Perovskite oxides have emerged as promising OER electrocatalysts due to their versatile physicochemical properties and high intrinsic activities. However, concerns persist regarding their structural stability and long-term electrochemical performance. Consequently, there is a pressing need for a highly active and structurally stable perovskite oxide electrocatalyst to enhance the overall performance of electrochemical energy storage devices, particularly zinc-air batteries.

In this work A-site management strategy is applied to tune the activity and stability of the double perovskite oxide. A range of double perovskite oxides was synthesized from La_2CoMnO_6 (LCM) up to Ba_2CoMnO_6 (BCM) by substituting Ba^{+2} with La^{+3}

to understand the origin of OER performance by investigating crystal structure, electronic structure, Fermi level, and work function. The crystal structure transitions from cubic to 2H hexagonal, while simultaneously observing a decrease in the work function with increasing levels of Ba incorporation. It suggests a relationship between crystal structure-oxygen vacancy-work function and activity for $Ba_xLa_{2-x}CoMnO_6$ (x = 0, 0.5, 1, 1.5, 2) double perovskite oxide electrocatalysts. The double perovskite oxide 2H-Ba_2CoMnO_6 demonstrates exceptional electrochemical performance and stands out as the most promising candidate for zinc-air battery applications. Notably, it displays a remarkable OER activity, characterized by a mere 288 mV overpotential at a current density of 10 mA cm^{-2}. Moreover, this material exhibits an extended period of stability, all the while maintaining its structural integrity without succumbing to instability concerns. This novel variety of double perovskite oxide not only showcases remarkable performance in terms of OER and battery applications, but it also serves as an elucidating model for comprehending the impact of crystal structure and work function on OER performance.

Keywords: Oxygen Evolution Reaction, Perovskite Oxide, Electrocatalyst, Zinc-Air Battery

ÖZ

ŞARJ EDİLEBİLİR ÇİNKO HAVA BATARYALARI İÇİN A-BÖLGESİ TASARLANMIŞ ÇİFT PEROVSKİT OKSİT HAVA ELEKTRODU

Erdil, Tuncay
Yüksek Lisans, Metalurji ve Malzeme Mühendisliği
Tez Yöneticisi: Dr. Öğr. Üyesi Çiğdem Toparlı

Eylül 2023, 88 sayfa

Yenilenebilir metal-hava bataryaları, su elektrolizörleri ve yakıt hücreleri gibi elektrokimyasal enerji depolama ve dönüşüm cihazları büyük ölçüde oksijen evrim reaksiyonu (OER) ve oksijen redüksiyon reaksiyonuna (ORR) bağlıdır. OER oldukça yavaş bir kinetiğe sahiptir ve bu yüzden bu cihazların verimliliğini engellemektedir. Perovskit oksitler değiştirebilir fizikokimyasal özellikleri ve yüksek içsel aktiviteleri sebebiyle gelecek vadeden OER elektrokatalizörlerinden biridir. Ancak, yapısal kararlılıkları ve uzun süreli elektrokimyasal stabiliteleri tartışmalıdır. Bu yüzden elektrokimyasal enerji depolama cihazlarının, özellikle çinko-hava bataryalarının, performansını geliştirmek için yüksek aktiviteye sahip ve yapısal olarak kararlı perovskit oksitlere ihtiyaç vardır.

Bu çalışmada A tarafı yönetim stratejisi uygulanarak çift perovskit oksitlerin aktivite ve stabilitesi ayarlanılmıştır. OER performansını anlamak için La_2CoMnO_6 (LCM)'den başlayarak Ba_2CoMnO_6 (BCM)'ye kadar çeşitli perovskit oksitler Ba^{+2}/La^{+3} değişikliği ile üretilerek kristal yapıları, elektronik yapıları, Fermi seviyeleri ve iş fonksiyonları incelenmiştir. Ba miktarıyla birlikte kristal yapı

kübikten 2H altıgene dönmüştür ve iş fonksiyonu giderek azalmıştır. $Ba_xLa_{2-x}CoMnO_6$ (x = 0, 0.5, 1, 1.5, 2) çift perovskit oksit elektrokatalistleri için kristal yapı-oksijen boşluğu-iş fonksiyonu ve aktivite arasında bir ilişki olduğu önerilmektedir. 2H-Ba_2CoMnO_6 çift perovskit oksidi en iyi elektrokimyasal performans ve çinko-hava bataryası sonuçlarına sahip olmakla birlikte 10 mA cm^{-2} de 288 mV aşırı potansiyele sahiptir ve yapısal kararsızlık olmadan uzun süreli stabiliteyle yüksek bir OER aktivitesi göstermektedir. Bu yeni tip çift perovskite oksit yalnızca üstün OER ve batarya performansı göstermekle kalmamış ayrıca kristal yapı ve iş fonksiyonunun OER performansı üzerindeki etkisini de açıklamaya yardımcı olmuştur.

Anahtar Kelimeler: Oksijen Oluşum Reaksiyonu, Perovskit Oksit, Elektrokatalizör, Çinko-Hava Bataryası

Dedicated to my beloved family…

ACKNOWLEDGMENTS

I want to express my heartfelt gratitude primarily to my advisor, Assist. Prof. Dr. Çiğdem Toparlı, for her unwavering backing, trust, and continuous encouragement in both my research and day-to-day endeavors. Her valuable insights have consistently enriched my thesis, and I feel immense joy and thankfulness for the opportunity to collaborate with her. Throughout my academic journey, she has been a guide, and without her support, the completion of this thesis would have been an insurmountable task.

I would also like to express my gratitude to my labmates, Uygar Geyikçi, Kasım Erdem Erik, Burçay Coşkuner and my friend Cansu Aygüzer. Their consistent assistance during my experiments has been invaluable. They were not merely colleagues in the lab; they became cherished friends with whom I shared enjoyable moments. I consider myself fortunate to have such wonderful labmates. Additionally, I wish to express my profound thanks to Çağla Özgür. Her unwavering support throughout my master's studies, marked by insightful scientific conversations and genuine friendship, has been incredibly motivating.

I am thankful to Prof. Dr. Yunus Eren Kalay and Can Okuyucu from Metallurgical and Materials Engineering Department for their help for my TEM analysis. Also, I would like to thank Dr. İlker Yıldız from METU Central Laboratory for his guidance and advice on the XPS analysis.

I want to offer a special acknowledgment to my closest friends, Abdullah Acar and Mervan Yılmaz. Your constant encouragement and unwavering support have been invaluable both in my personal journey and professional endeavors. Whenever I felt exhausted or on the verge of giving up, your words of encouragement pushed me forward, and your ability to bring laughter into even the toughest moments has been a true blessing.

Finally, I want to convey my profound and utmost gratitude to my family, without whom I wouldn't be the person I am today. I owe an immeasurable debt of thanks to my parents, Nusret and Zeynep Erdil, as well as my sisters Gülten and Gülden Erdil, and my brothers Barış and Güven Erdil, for their unwavering love and support that have been a constant presence throughout my life.

TABLE OF CONTENTS

LIST OF TABLES

TABLES

LIST OF FIGURES

FIGURES

CHAPTER 1

INTRODUCTION

The development of clean and renewable energy storage and conversion devices is crucial in mitigating climate change[1–3]. Within the realm of emerging technologies aimed at tackling climate change, water electrolyzers, regenerative fuel cells, and rechargeable metal-air batteries are emerging as prominent and impactful solutions [4–9]. These devices are reliant on oxygen/hydrogen evolution and reduction reactions, for which the utilization of catalysts capable of sustaining prolonged operation and achieving high efficiency within alkaline environments is imperative [10–13]. The oxygen evolution reaction (OER) constitutes a pivotal and determining phase in these systems. Nonetheless, the OER presents sluggish kinetics attributed to its intricate four-step mechanism, which encompasses the transfer of numerous electrons and protons [10,14–21]. Extensive research has been conducted to reduce the anodic overpotential during the OER by exploring various electrocatalysts. Currently, IrO_2 and RuO_2 are considered state-of-the-art OER electrocatalysts [22–25]. However, the widespread adoption of these technologies for large-scale applications is impeded by their substantial cost, restricted availability of materials, and inadequate long-term stability.

Numerous economically viable and efficient OER electrocatalysts have been documented to date, encompassing metal oxides, carbon-based materials, chalcogenides, and perovskite oxides [26–31]. Within this array of options, perovskite oxides stand out as prominent and robust electrocatalysts. This distinction is attributed to their capacity for tuning A and B sites, along with their advantageous physicochemical characteristics. Perovskite oxides exhibit a structural configuration denoted as ABO_3, wherein the A-site accommodates alkaline, alkaline earth, lanthanides, or actinides, while the B-site houses 3d transition metals. Notably, the crystal and electronic structures of perovskite oxides can be systematically adjusted

by modifying either the A-site or the B-site components [32–36]. Therefore, perovskite oxide electrocatalysts present proof to explain the relationship between the nature of the material and the electrochemical performance Multiple reports have consistently indicated that the OER activity of perovskite oxide electrocatalysts is commonly associated with the electronic structure of the B-site metal, the presence of oxygen vacancies, and the involvement of lattice oxygen in the reaction mechanism [14,37–45]. Indeed, strategies that involve manipulation of the B-site element lead to modifications in the OER activity [46–50]. A-site management strategy is explored less compared to substituting the B-site element for improving the electrocatalyst's OER activity and long-term stability. The A-site substitution between trivalent and divalent cations can cause the changing and arrangement of the charge balance, leading to vacancy formation [35,42,51–54]. For example, incorporating Sr^{2+} at the A-site of $LaNiMnO_3$ induces Ni^{3+} states, this manipulation causes an upward shift in the occupied valence band center and enhances the hybridization between O 2p and metal 3d orbitals [55]. Also, Sr doping into $LaCoO_3$ caused an increase in electrical conductivity and changed the OER mechanism [35]. However, Sr at the A-site leads to segregation during the long-term electrochemical test and causes structural instability and surface reconstruction [56–58]. Moreover, a well-known catalyst, $Ba_{0.5}Sr_{0.5}Co_{0.8}Fe_{0.2}O_{3-\delta}$ (BSCF), also suffer from structural instability; it becomes amorphous under long-term OER condition [38,59]. Ba is an attractive choice for the divalent A-site cation because it has a large ionic radius among the divalent cations, and due to that, it forms the hexagonal perovskite oxide structure. The primary distinction between the hexagonal and cubic crystal structures lies in the arrangement of B-cations. In the cubic structure, B-cations are exclusively corner-shared. However, in the hexagonal structure, B-site cations are linked to both corner-shared and face-sharing octahedral sites. Notably, the 2H hexagonal structure exclusively features face-sharing octahedral points. Theoretical calculations have demonstrated the crucial role played by face-sharing octahedral sites in driving the heightened OER activity of hexagonal perovskite oxides compared to their cubic counterparts [60–65]. Also, the presence of larger A-site cations, like Ba, results in

an augmentation of the oxygen-metal bond angle. This alteration contributes to an enhancement in electrical conductivity, thereby leading to improved OER activity.

In this thesis, an A-site management strategy has been applied to the La_2CoMnO_6 to improve the OER activity by substituting La with Ba. Thus, A previously unattainable 2H-$Ba_2CoMnO_{6-\delta}$ (BCM) double perovskite oxide is successfully synthesized using a novel air-quenching method. BCM showcases outstanding OER performance, achieving an impressive overpotential of 288 mV at a current density of 10 mA cm^{-2}. Furthermore, its crystal structure and OER activity remain unchanged even after undergoing extensive long-term electrochemical testing for over 60 hours in a 0.1 M KOH environment. The stability of the crystal and electronic structures was assessed through high-resolution transmission electron microscopy (HRTEM) and X-ray photoelectron spectroscopy (XPS) after a 60-hour testing period. To explain the OER performance of the electrocatalyst experimental work function values, oxygen vacancy variation, and crystal structure change are consideredThese investigations indicate the promising potential of employing the A-site management strategy to enhance both the OER activity and structural stability of perovskite oxides. This approach can have an impact by influencing factors such as crystal structure, work function, charge balance, and the presence of oxygen vacancies.

CHAPTER 2

LITERATURE REVIEW

2.1 Metal-Air Batteries

The lithium-ion batteries (LİBs) have exhibited extraordinary developments in the past decades. This approved battery technology is used in everyday applications, from mobile phones to electric vehicles, due to high energy efficiency and long cycling stability [66,67]. However, global lithium scarcity is currently evident, with the element being increasingly scarce in contemporary times. Additionally, a formidable challenge exists to recycle lithium [68–70]. Therefore, higher energy-density electrochemical systems are needed to ensure the requirements of these new technologies. Metal-air batteries are promising candidates due to their relatively high specific energy and volumetric energy density comparable to other batteries. Among the metal-air batteries, Zn-air batteries (ZABs) step forward. ZABs are inexpensive, abundant, environmentally friendly, have high theoretical specific energy, and have a long shelf-life [1,12,13,71].

2.1.1 Zinc-Air Batteries

Zinc-air batteries are composed of three essential components: a zinc metal anode, an aqueous alkaline electrolyte, and an air electrode cathode that is permeable to both air and O_2 gas, Figure 2.1. ZABs are categorized into three primary types: primary batteries, secondary batteries, and mechanically rechargeable batteries. Primary batteries are used only once and are disposable zinc-air batteries, and they are not rechargeable; thus, only zinc and electrolyte control the battery performance.

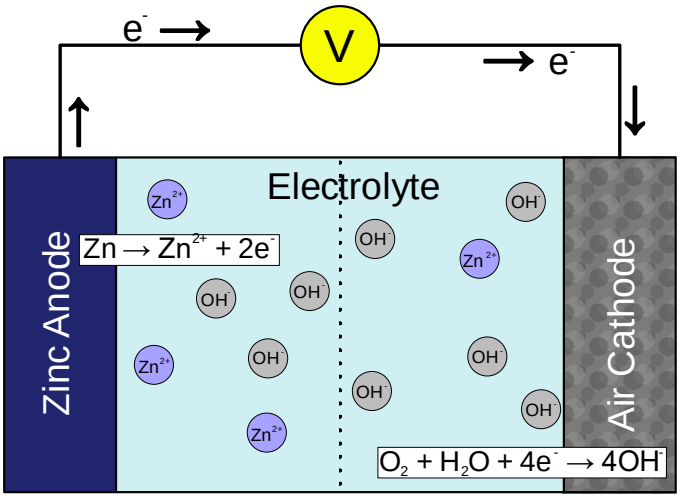

Figure 2.1 Schematic representation of a Zinc-Air battery.

Conversely, the longevity of mechanically rechargeable zinc-air batteries hinges on the performance of the air cathode, as the zinc anode and electrolyte can be replenished. The secondary zinc-air battery relies on a reversible zinc anode and efficient bifunctional catalyst. The oxygen pressure gradient between the external environment and the battery interior causes the diffusion of oxygen through the porous carbon air electrode into the cell. Thus, the oxygen is reduced to hydroxyl ions with the help of catalysts accompanied by zinc oxidation at the anode side. Then, generated hydroxyl ions migrate from the cathode to the anode, facilitating the completion of the cell reaction. The reactions occurring during the charging and discharging processes at the anode and cathode sections of the battery are as follows[72]:

During discharging:

Zn-Anode: $Zn + 4OH^- \rightarrow Zn(OH)_4^{2-} + 2e^- \ (E^0 = 1.25\ V)$ (2.1)

$Zn(OH)_4^{2-} \rightarrow ZnO + H_2O + 2OH^-$ (2.2)

Air Cathode: $O_2 + 4e^- + 2H_2O \leftrightarrow 4OH^- \ (E^0 = 0.4\ V)\ (ORR)$ (2.3)

Overall: $2Zn + O_2 \rightarrow 2ZnO \ (E^0 = 1.65\ V)$ (2.4)

During charging:

Zn-Anode: $ZnO + H_2O + 2OH^- \rightarrow Zn(OH)_4^{2-}$ (2.5)

$Zn(OH)_4^{2-} + 2e^- \rightarrow Zn + 4OH^-$ (2.6)

Air Cathode: $2OH^- \leftrightarrow \frac{1}{2}O_2 + 2e^- + H_2O\ (OER)$ (2.7)

Overall: $ZnO \rightarrow Zn + \frac{1}{2}O_2$ (2.8)

From the chemical equations above, the equilibrium potential of the ZAB should be 1.65 V. Still, the working voltage is less than 1.65 V because of the activation, ohmic resistance, and concentration internal losses.

2.1.1.1 Anode

The ZAB has a pure zinc metal anode, and the zinc oxidizes during discharge, and zinc oxide transforms pure metal zinc during charge. Therefore, many research focuses on the air cathode electrode, especially the catalyst part of the electrode. The zinc anode is responsible for high-efficiency recharging, high specific capacity/energy, and maintaining capacity over long charge and discharge cycles. Some limiting factors obstruct the performance of the zinc electrode. These are hydrogen evolution, dendrite growth, shape change, and passivation.

The zinc corrosion produces H_2 with respect to equation [73,74]:

$$Zn + 2H_2O \rightarrow Zn(OH)_2 + H_2 \text{ (Hydroggen evalutaion reaction (HER))} \quad (2.9)$$

The HER retard the coulombic efficiency of the zinc electrode. Also, HER consumes some of the electrons during charging. Therefore, the HER should be hindered to avoid zinc electrode consumption; in this way, zinc metal will be completely consumed during discharge without zinc corrosion and passivation and cause an increase in the capacity of the battery [75–77].

The zinc dendrites form during the charging step. These dendrites are needle-like, sharp, metallic ledges [78,79]. They break off from the anode electrode and result in capacity loss, or more crucially, it perforates the separator and touches the cathode, causing a short circuit. Many studies show that zinc reduction overpotential is the crucial parameter of zinc dendrite formation [1,80,81]. The lower overpotentials are prone to produce different morphologies, such as epitaxial, sponge, or boulder types [78,79]. However, dendritic structures can also develop at lower zinc reduction overpotentials when the initiation time is prolonged due to repeated dissolution and deposition cycles.

The shape change is another limited factor. During discharge, zinc dissolves into the electrolyte, while during charging, it accumulates at various points on the anode. After undergoing multiple charge and discharge cycles, this accumulation and segregation lead to uneven current distribution and a decrease in capacity [82,83].

The passive layer is insulating and cannot be discharged anymore. This layer hinders the motion of the OH^- ions and discharge products. The formation of a passive ZnO layer occurs when the solubility limit of $Zn(OH)_4^{2-}$ is reached, causing ZnO to precipitate onto the surface of the zinc electrode. This layer impedes the discharge reactions from progressing [84,85]. Also, the presence of the ZnO layer raises the resistance of the zinc anode, leading to a loss of discharge voltage and an elevation in charge voltage.

Increasing the electrode thickness promotes the passivation of the zinc electrode, favoring the formation of ZnO over $Zn(OH)_4^{2-}$. [84,86].

These limitations can also interplay with each other. For instance, changes in shape can diminish the active surface area of the zinc anode, resulting in an elevation of zinc reduction overpotential. Consequently, zinc dendrites may form, and zinc passivation can induce dendritic growth due to the same underlying reason. Therefore, the solution to one limitation can trigger the mitigation of other limitations directly or indirectly.

There are various strategies to retard these limitations and improve the performance of the zinc electrode. These strategies can improve the cycle life, coulombic efficiency, and capacity of the battery. This thesis considers the electrocatalyst effect on the OER and the improvement of the ZAB cathode. Thus, the strategies for improving the performance of zinc electrodes are briefly mentioned in this section because it is a different research area to focus on enhancing zinc anode to upshift the performance.

The extensive surface area of the zinc electrode mitigates the reduction overpotential of zinc, thereby impeding the formation of dendrites during the charging process. Also, zinc passivation can be prevented by allowing the distribution of the current and electrolyte through the three dimensions of the zinc electrode, such as the 3D electrode structure [87–89]. However, increasing surface area causes an increase in the hydrogen evolution rate due to high exposing area.

Heavy-metal or carbon-based materials are the common additives of the zinc electrode. These materials improve the conductivity and chemical resistance to the alkaline environment, which helps to prevent zinc oxide passivation on the anode surface [90]. Bi, In, and Pb are the most common heavy-metal additives. These additives can help to reduce dendritic growth, shape change, hydrogen evolution, and passivation [91–93]. These additives should be homogenously distributed with an adequate amount; otherwise, they cause a capacity loss.

Discharge-trapping additives can also be beneficial for reducing dendritic growth. These additives trap the $Zn(OH)_4^{2-}$ discharge product [94]. Ca [95] and Al [96] are the examples of the discharge-trapping additives.

The most applying and straightforward strategy is coating. The zinc electrode or zinc powders can be coated to improve the long-term cyclic life of the ZAB. The coatings allow the movement of the OH^- ions and reduce the $Zn(OH)_4^{2-}$ movement or total blocks. This reduction smooths down the shape change and reduces the concentration gradient [97–99].

2.1.1.2 Electrolyte

The electrolyte serves as the medium for ionic migration, allowing OH- ions to travel from the zinc anode to the cathode across the electrolyte during both the charge and discharge cycles. Commonly employed alkaline electrolytes include potassium hydroxide, sodium hydroxide, and lithium hydroxide [100]. KOH steps forward due to its high ionic conductivity (~640 mS cm^{-1}) [101]. KOH exhibits maximum conductivity at 6 M concentration; so, in batteries, generally, this concentration is used [102]. Raising the concentration of KOH diminishes the resistance of the electrolyte, although excessively high concentrations can lead to elevated electrolyte viscosity. The alkaline KOH electrolyte is very sensitive to CO_2 because the battery is operated under ambient air. The CO_2 reacts with OH^- and forms carbonates; thus, the OH^- concentration decreases. As an instance, the elevated concentration of CO_2 in the atmosphere impacts the bifunctional air electrode, leading to decreased performance and shortened electrode lifespan. This is attributed to the precipitation of carbonates within the electrode's pores, obstructing the entry of air and oxygen [103–105]. Some electrolyte additives, such as $Zn(OAc)_2$, can be added to suppress these obstacles. Aqueous alkaline electrolytes are predominantly employed in ZABs owing to their notable ionic conductivity and favorable interfacial properties between the electrodes and the electrolyte. Non-aqueous solid electrolytes can serve as alternatives, yet it's important to note that solid electrolytes generally exhibit

diminished energy efficiency and lower power performance compared to their aqueous counterparts. Solid electrolytes allow zinc-air batteries to become portable and flexible with various shapes [106–109]. However, solid electrolyte causes a challenging electrode-electrolyte interface because in an aqueous electrolyte, the catalyst layer, for example, is fully covered with aqueous electrolyte but the solid electrolyte just contact with the surface of the catalyst layer and does not cover or penetrate the catalyst layer. This results in high interfacial resistance, leading to a low current rate and high overpotential during charging and discharging [105,110,111].

2.1.1.3 Cathode

The cathode of the ZAB is responsible for bifunctional oxygen electrochemistry. The bifunctional electrode reduces oxygen during discharging and evolves oxygen reversely during charging. The bifunctional catalysts affect the zinc-air batteries' power performance, long-term cyclic charge-discharge, and coulombic efficiency. The development of highly active bifunctional air electrodes is quite challenging because both oxygen reactions, i.e., OER and ORR, have high overpotentials; both are sluggish and consist of many steps [33,112–115]. Therefore, a significant bifunctional electrocatalyst can promote both OER and ORR. Also, it should be stable under highly oxidative (OER) and highly reducing (ORR) conditions at considerably high current rates. Also, the bifunctional electrocatalyst must withstand a voltage range between ~0.8 V during discharging and ~2.2 V during charging [1,6,12,13,80,116]. Implementing a divided electrocatalyst setup for separate OER and ORR processes can enhance the cyclic stability of the battery over the long term. However, this approach inherently introduces greater intricacy to the battery design, resulting in increased weight and volume, which subsequently impacts the power and energy densities negatively. A common bifunctional electrode configuration includes a hydrophobic gas diffusion layer (GDL) and a catalyst layer with moderate hydrophilicity. This catalyst layer plays a critical role in catalyzing the oxygen

reactions and enhancing the overall battery performance in aspects such as cycle life, specific capacity, energy density, power density, and coulombic efficiency. The primary purpose of the GDL is to support the catalyst physically and conductively and allow oxygen diffusion during discharging and charging. The OER happens at the interface between the electrolyte and solid catalyst (forming a two-phase reaction zone), whereas the ORR takes place at the three-phase interface involving oxygen, the electrolyte, and the catalyst. Therefore, creating a bifunctional electrode with the right degree of hydrophilicity is essential to prevent excessive wetting or drying of the active catalytic sites, ensuring optimal performance of the catalyst.

The gas diffusion layer crucially affects the battery performance by supporting the bifunctional electrocatalyst physically and electrically. The functions of the gas diffusion layer are essential for maintaining the battery's performance. The GDL physically supports the catalyst and avoids the leakage of the electrolyte by acting as a hydrophilic wet-proofing electrode. Also, the GDL permits the ingress and egress of oxygen gas, while also functioning as a conduit for electrical conduction between the current collector and the electrode. The GDL should possess characteristics of being thin, porous, and hydrophobic, in order to facilitate the movement of oxygen while minimizing the likelihood of electrolyte leakage. The hydrophobicity is generally provided by coating or grafting the GDL with PTFE, PVDF, PE, and FEP [117–119]. It is wanted that GDL should perform rapid oxygen diffusion, high structural integrity, excellent electrical conductivity, also strong electrochemical stability, and chemical durability.

The sluggish kinetics of both OER and ORR necessitate the use of bifunctional catalysts to enhance the efficiency of these electrochemical oxygen reactions. Nowadays, IrO_2 and RuO_2 are efficient OER electrocatalysts, but their ORR performance is poor. On the other hand, Pt or Pt/C is excellent for the ORR but performs poor OER performance [120]. Also these precious catalysts suffer from limitations in terms of structural and chemical stability. Additionally, their high cost, limited availability, and poor long-term stability pose challenges for their widespread utilization in large-scale applications. Therefore, developing robust and

economically viable new bifunctional electrocatalysts is crucial to accelerate the utilization of zinc-air batteries. However, due to the OER and ORR having different operating ranges during the discharge and charge processes, obtaining an efficient bifunctional catalyst with chemically and structurally stable is challenging. Significant progress has been made in the field of bifunctional catalyst development, encompassing materials derived from transition metals, including oxides, perovskites [33,34,36,54,116,121–124], chalcogenides [125–129], nitrides [130–132], and carbides [133–135]. Furthermore, research has explored heteroatom-doped carbon nanomaterials and hybrid materials [136–138] that combine the attributes of both types. The mechanisms and kinetics of OER and ORR are intricate and challenging to foresee, often necessitating the trial-and-error approach in catalyst development. Regarding ORR, two distinct reaction pathways are observed for the reduction of oxygen in aqueous environments: the direct four-electron pathway and the two-electron pathway [114,139,140]:

$$O_2 + 2H_2O + 4e^- \leftrightarrow 4OH^- \quad (2.10)$$

$$O_2 + H_2O + 2e^- \leftrightarrow HO_2^- + OH^- \quad (2.11)$$

The ORR process typically exhibits a preference for the direct four-electron reduction pathway, leading to the conversion of oxygen into OH- without producing peroxide in the solution [114,120,141]. This outcome is advantageous in terms of desired reaction products. Noble metal catalysts, perovskite oxides, high entropy oxides, and nitrogen-doped carbon catalysts are favored for facilitating the direct four-electron reduction pathway. On the other hand, the two-electron pathway release peroxide species, and these peroxide species buildups hinder ORR's efficiency and poison the catalyst and GDL due to its high oxidizability.

The OER reaction mechanism pathways and kinetics are more unclear and hard to be determined. The reverse process of the ORR direct-four electron pathway is the commonly accepted mechanism for metal-catalyzed OER. As aforementioned, noble metal oxide catalysts have superior OER activity and very high electrical conductivity, but these catalysts are expensive and scarce, and their long-term

stability is not enough. Therefore, the transition metal oxides and/or (oxy)hydroxides can be the alternative catalysts because of their long-term structural and chemical stability and abundance. The perovskite and spinel-type oxides, e.g., lanthanum nickel oxide, barium-lanthanum cobalt manganese oxide, high-entropy spinel oxide, and nickel/cobalt oxide, exhibit semiconducting properties and thus demonstrate high OER performance.

These catalysts have surface metal active sites (M*) for the OER, these metal active sites react with OH^- ions in four stages given below, and at the end of these stages, O_2 evolves [114,142,143].

$$M^* + OH^- \rightarrow M\text{-}OH \quad (2.12)$$

$$M\text{-}OH + OH^- \rightarrow M\text{-}O + H_2O \quad (2.13)$$

$$M\text{-}O + OH^- \rightarrow M\text{-}OOH \quad (2.14)$$

$$M\text{-}OOH + OH^- \rightarrow M^* + O_2 + H_2O \quad (2.15)$$

In the last stage, the O_2 evolves, and the metal active site is recovered with water. The transition metal-oxygen binding strength determines the rate-determining step for overall OER performance. The rate-determining step of the OER can be enhanced by adjusting the structural, compositional, geometric, and electronic properties of the electrocatalyst. Certain descriptors used to explain the OER activity encompass the O p-band center position in relation to the Fermi level, work function, e_g orbital occupancy, metal-oxygen covalency, and oxygen vacancy content [39,62,144–146]. However, these trends are intricate and often interconnected. As a result, factors such as electronic structure, chemical composition, electrochemically active surface area, surface composition, and electrical conductivity play crucial roles in determining these descriptors. The catalytic active sites, selectivity, i.e., minimizing unwanted products, and stability are the critical parameters of a bifunctional electrocatalyst.

The catalytic active sites play a pivotal role in facilitating the adsorption of reaction intermediates on the surface and aiding in the migration of ions. Selectivity

minimizes undesirable products such as peroxide and OH^- and O_2 for ORR and OER, respectively. Therefore, an efficient bifunctional electrocatalyst can selectively catalyze oxygen via a direct four-electron transfer process during ORR, hindering CO_2 evolution during OER. The bifunctional electrocatalyst should be stable under harsh alkaline conditions and also withstands highly oxidative OER and highly reductive ORR conditions at different current rates. The phase/crystal structure change, surface passivation, material degradation, and segregation can cause stability loss.

The catalytic activity of the electrocatalyst is significantly influenced by factors such as crystal structure, stoichiometry, particle size, and morphology. The drastic effect of the crystal structure is observed clearly when the crystal structure changes from cubic to hexagonal. $Ba_{0.5}Sr_{0.5}Co_{0.8}Fe_{0.2}O_{3-\delta}$ (BSCF) is a widely recognized cubic perovskite electrocatalyst that has demonstrated OER performance approximately one order of magnitude higher than commercial IrO_2 in alkaline media [59,61,64]. When the crystal structure of the BSCF changes to hexagonal [61,64], BSCF shows even superior OER activity than cubic BSCF. Also, 6H-$SrIrO_3$ perovskite oxide with a hexagonal crystal structure has been identified as an excellent OER electrocatalyst in acidic media [147]. Furthermore, the incorporation of Ir into BSCF facilitates the movement of the O p-band center towards the Fermi level [64]The valence of cobalt in hexagonal perovskite structures is typically higher than in cubic perovskite structures, as observed in the BSCF system. This difference arises due to the B-site transition metal-oxygen bond distances in the hexagonal crystal structure being smaller in face-sharing octahedral sites compared to the corner-sharing octahedral sites in the cubic crystal structure. The enhanced OER activity of hexagonal perovskite oxides is attributed to the presence of the face-sharing octahedral units. In hexagonal structures, B-site cations are connected to face-sharing octahedral sites, unlike in cubic structures where they are connected solely to corner-sharing points. This distinction in connectivity contributes to the superior OER performance observed in hexagonal perovskite oxides. Theoretical calculations have revealed that the presence of face-sharing octahedral sites plays a crucial role in the significantly

enhanced OER activity exhibited by hexagonal perovskite oxides compared to their cubic counterparts. This structural arrangement provides a favorable environment for catalytic activity, contributing to the superior OER performance of hexagonal perovskite oxides.

The stoichiometry and composition of an electrocatalyst are crucial for its catalytic activity and selectivity. These factors determine its ability to facilitate specific electrochemical reactions by affecting its electronic structure, active site availability, and surface properties. For example, A-site or B-site substitution in perovskite oxides strongly affects catalyst performance. Substituting Sr for La in $LaCoO_3$ enhances electrical conductivity and OER performance. This substitution shifts the OER mechanism from adsorbate evolution mechanism (AEM) to lattice-oxygen-mediated mechanism (LOM) [35]. Incorporating Sr into $LaNiO_3$ introduces Ni^{3+} states, elevating the occupied valence band center and enhancing the hybridization of O 2p with metal 3d orbitals. [55]. These electronic characteristics facilitate the exchange of O^{2-} / OH^- ions, thereby promoting bifunctional catalytic activity for both the ORR and OER. However, incorporating Sr at the A-site may lead to the segregation of Sr-rich regions and surface reconstruction during electrochemical reactions. These phenomena can potentially disrupt the bifunctional electrocatalyst's performance in both OER and ORR reactions.

The size of the electrocatalyst particles affects the catalytic reactivity, electrical conductivity, and surface area. The nanosized catalyst particles have significantly different physical and chemical properties than larger (bulk) particles due to quantum effects. The nanosized particles have higher specific catalytic activity due to the absence of geometric size-induced strain. Morphology, like particle size, significantly impacts the catalytic activity of an electrocatalyst. The different morphologies, such as 3D-honeycomb, 3D-mesoporous, nanofibers, and core shells, directly or indirectly affect the catalytically active surface area and enhance the performance of the OER and ORR of the bifunctional electrocatalyst [148,149].

2.1.2 Electrochemistry of Batteries

Sustainable energy devices, especially energy storage and conversion applications, operate via chemical energy-electrical energy conversion. These conversion processes heavily depend on electrochemical reactions. In the case of zinc-air batteries, these electrochemical reactions are OER and ORR. A significant increase in overpotential is necessary to initiate OER and ORR, resulting in additional energy input during energy storage and reduced energy output during energy conversion, as shown in Figure 2.2. Therefore, developing highly active and stable materials for catalyzing electrochemical reactions is challenging and essential. The OER and ORR are based on O_2/H_2O redox couple equilibrium.

The below Nernst equation gives the equilibrium. The standard equilibrium potential for forming oxygen from water is $E^0_{O_2/H_2O} = 1.229\ V\ vs.\ RHE$ [114,150].

$$2H_2O \leftrightarrow O_2 + 4H^+ + 4e^- \tag{2.16}$$

$$E_{O_2/H_2O} = E^0_{O_2/H_2O} - \frac{RF}{4F} ln \frac{a^2_{H_2O}}{a_{O_2} a^4_{H^+}} \tag{2.17}$$

$$O_2 + 2H^+ + 2e^- \leftrightarrow H_2O_2 \tag{2.18}$$

$$H_2O_2 + 2H^+ + 2e^- \leftrightarrow 2H_2O \tag{2.19}$$

$$E_{O_2/H_2O_2} = E^0_{O_2/H_2O_2} - \frac{RF}{2F} ln \frac{a_{H_2O_2}}{a_{O_2} a^2_{H^+}} \tag{2.20}$$

$$E_{H_2O_2/H_2O} = E^0_{H_2O_2/H_2O} - \frac{RF}{2F} ln \frac{a^2_{H_2O}}{a_{H_2O_2} a^2_{H^+}} \tag{2.21}$$

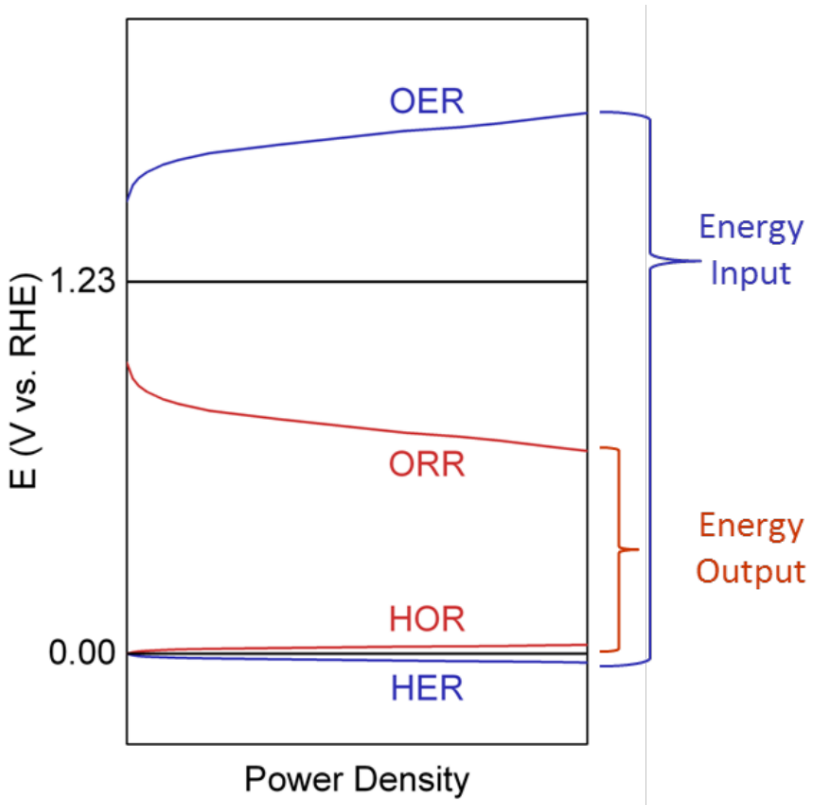

Figure 2.2 The graph displays the relationship between voltage and power density for the processes of water splitting (indicated by the blue line) and battery operation (indicated by the red line).

The given equations are the overall expression of the OER and ORR. There are several principal steps during OER and ORR, for example, four-electron and proton transfer, bond-breaking ORR step, or bond-forming OER. The OER and ORR mechanisms can be combined in three stages[114,150–152]:

1) The dissociation mechanism of ORR and the recombination mechanism of the OER (reverse): the oxygen O-O bond is broken during adsorption, and O^{ads} are reduced to OH^{ads} and H_2O^{ads}; the reverse of this mechanism is OER recombination.
2) The association mechanism of ORR and OER: the OOH^{ads} breaks into O^{ads} and OH^{ads} during ORR, or OOH^{ads} form from O^{ads} and OH^{ads} during OER.

3) In addition, step, when the two-electron transfer step takes place during ORR, the peroxo mechanism is activated and leads to the formation of OOH^{ads} and $HOOH^{ads}$, then breaks into OH^{ads}; the reverse mechanism is the peroxo mechanism for OER.

These formed adsorbed oxygenated species are the significative elements to determine the performance of electrocatalysts. These processes occur during the OER and ORR reactions on the surfaces of transition-metal catalysts. Indeed, a correlation has been established between the adsorption energy of oxygenated species on the surface of a transition-metal and the position of the d-band center relative to the Fermi level, known as the d-band center model. The d-band center model proposes that when there is a larger separation between the Fermi level and the d-band center, the strength of the metal-adsorbate oxygen ($M\text{-}O^{ads}$) bond tends to decrease.

2.1.2.1 Oxygen Evolution Reaction (OER)

The OER is an electrochemical process where water molecules are oxidized at the anode to produce oxygen gas and H^+ ions. A visual representation of the OER cycle can be observed in Figure 2.3. OER plays a crucial role in the overall process of water splitting. Oxygen evolution reaction has sluggish kinetics; therefore, improving catalysts to enhance the performance and upshift the kinetics of OER is necessary. The OER takes place on oxidized surfaces [153–155]. The absorption of OOH and O limits the progress of the OER. The overpotential is an important factor for evaluating the electrocatalyst OER performance. The overpotential is the deviation from the reversible oxygen potential (1.23 V) that occurs at a current density of 10 mA cm^{-2}. Also, the difference between O and OH binding energies is another catalytic descriptor. The Sabatier principle suggests that the highest catalytic activity is attained with an optimal binding energy difference.

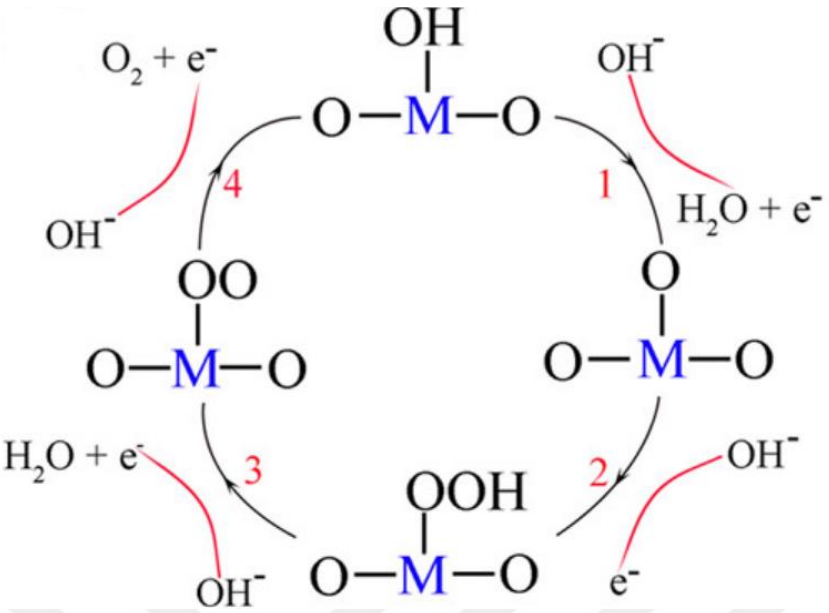

Figure 2.3 Diagram illustrating the four-step process of the oxygen evolution reaction [123].

The electrocatalyst's inner surface becomes active as the oxygen evolution reaction leads to an elevated overpressure at the electrode-electrolyte interface. This is one of the distinct properties of OER over ORR because in ORR, only the outer surface of the electrocatalyst is active, and diffusion limits the reduction when overpotential increases [114,142]. Therefore, the porosity of the electrocatalyst should be considered for OER because the inner part of the electrocatalyst becomes active during the reaction. Moreover, formed O_2 bubbles during OER can attach to the active sites and block the active sites, decreasing the efficiency; thus, detachment of O_2 bubbles is an essential feature for electrocatalysts. The rapid oxygen evolution rate results in oxygen gas saturation at the solid-liquid interface, preventing complete dissolution of some O2 molecules. These bubbles act as a sink for newly formed gasses and obstruct the electrochemically active areas. One of the promising strategies for increasing the detachment of gas bubbles is accelerating the O_2 evolution to decrease overpotential. However, the stability of the catalysts to continuously evolve O_2 is challenging.

Commercial IrO_2 and RuO_2 exhibit limited long-term stability (2-4 hours) in alkaline conditions. As a result, perovskite, Ruddlesden-Popper, and spinel-type oxides are considered promising electrocatalysts that can sustain OER in alkaline media for extended periods.

2.1.2.2 Oxygen Reduction Reaction (ORR)

The oxygen reduction reaction (ORR) is a fundamental electrochemical process of significant importance in a variety of energy storage and conversion devices. The ORR involves the reduction of O_2 gas to water or OH^-. The mechanism of the ORR encompasses multiple stages, comprising the binding of oxygen molecules onto the cathode surface, the transfer of electrons from the cathode to the oxygen molecules, and the subsequent generation of hydroxide ionsThe ORR is a intricate process that is impacted by a range of elements, including the characteristics of the electrode material, the composition of the electrolyte, and the conditions under which the electrochemical system operates.

The ORR has a high energy barrier like the OER, so finding an efficient, long-term, cost-effective electrocatalyst is challenging. Platinum is the commercial electrocatalyst for ORR, but its high cost, scarcity, and poor long-term stability obstruct its usage [114,139,141,154]. Catalysts with ample surface area, like graphene, carbon nanotubes, and carbon black, can furnish active sites for the ORR. Additionally, the crystal structure's defect chemistry offers active sites for the ORR, enhancing electrochemical activity. Moreover, the crystal structure plays a pivotal role in determining the electrocatalytic activity of the ORR. For instance, hexagonal nanoparticles exhibit heightened ORR activity in both acidic and alkaline electrolytes, such as 0.1 M $HClO_4$, 0.5 M H_2SO_4, and 0.1 M KOH.

2.1.3 Electrocatalysts for OER/ORR

Electrochemical energy storage devices use chemical bonds to store energy. Water splitting stands as an optimal and environmentally friendly energy solution, notably contributing to energy storage through electrochemical means. This process of water splitting emerges as a fundamental electrochemical reaction with paramount importance. Energy is stored by forming H_2 and is released by reducing H_2. However, there are two crucial reactions, OER and ORR, and both have sluggish kinetics and high overpotentials. Therefore, designing efficient and reliable electrocatalysts for oxygen reactions is critical.

2.1.3.1 Platinum Group Catalysts

Platinum is the commercial ORR electrocatalyst because it activates the four-electron pathway. Pt has high mass activity and low overpotential, but its stability is very poor in alkaline electrolytes and is scarce and expensive. [156,157] Commercially, catalysts from the platinum group, including Pt, Ir, Ru, and Au, as well as their oxide derivatives, are commonly employed for electrocatalysis in both OER and ORR processes. Notably, IrO_2 and RuO_2 are recognized as exceptional OER electrocatalysts due to their remarkable attributes, including low overpotential and rapid kinetics. However, they are again scarce and expensive, so their widely used is obstructed. The ORR activity of platinum group metal oxide electrocatalyst is determined as Os > Ru > Ir > Pt > Au, and the stability of the catalysts to OER is Au > Pt > Ir > Ru >Os; there exists an inverse relationship between stability and activity [158]. Therefore, IrO_2 is the most commonly used electrocatalyst due to activity-stability balance. Whether these elements are very effective for bifunctional electrocatalysts, they are extremely expensive. Therefore, new feasible electrocatalysts are needed to boost oxygen electrochemistry. These new, very efficient electrocatalysts can be designed by considering material science methods. For example, different crystal structures, e.g., spinel, perovskite, rock-salt, or

different morphologies, e.g., nanoparticles, nanotubes, and heterojunctions, could be synthesized to upshift the performance of OER and ORR.

2.1.3.2 Perovskite Type Transition Metal Oxide Catalysts

Perovskite oxides are considered promising bifunctional electrocatalysts due to their adjustable physicochemical properties. The single perovskite oxide is represented as ABO_3, while the double perovskite oxide is denoted as $A_2BB'O_6$. In these structures, the A site typically comprises alkaline rare earth or lanthanide ions, and the B site is occupied by transition metal ions; Figure 2.4 represents the single and double perovskite oxides [36]. Lately, double perovskite oxides have captured considerable interest within the energy materials domain. This is attributed to their unanticipated and improved physicochemical properties, along with heightened intrinsic catalytic activities when contrasted with single perovskite oxide structures [65,121,122,159,160]. Also, double perovskite oxides have too many elemental combinations for maintaining charge balance. Perovskite oxides can be different crystal structures. The ideal crystal structure for single perovskite oxide is a cubic structure with Pm-3m space group. It consists of a BO_6 corner-sharing octahedral site, and A cations occur at the remaining holes; their symmetry is cuboctahedra [161]. Conversely, the crystal structure of double perovskite oxides hinges on the interplay between the charge and size disparities among B cations, dictating their arrangement. The variance in charge between B cations defines the specific crystal structure type. This charge difference contributes to three distinct crystal structures characterized as random, rock salt, and layered.

The first studies on single perovskite electrocatalysts were published during the 1970s. Several perovskite oxide compositions have been examined. $LaCoO_3$ has promising activity; Ni and Sr doping also improved the performance by increasing conductivity. The early studies on $LaNiO_{3-\delta}$ suggested the σ^* bond formed between the e_g orbitals of transition metal and adsorbate oxygen [141]. Various 3d transition metals ($LaMnO_3$, $LaCoO_3$, $LaFeO_3$, $BaCoO_3$, $BaMnO_3$, etc.) and A-site elements

(La, Sr, Ba, Pr, Nd, Sm, Gd, Eu, etc.) containing perovskite oxides have been studied as electrocatalyst. For example, different A-sites containing $AMnO_3$ were tested for ORR, and results show that when ionic radius increases, ORR activity also increases.

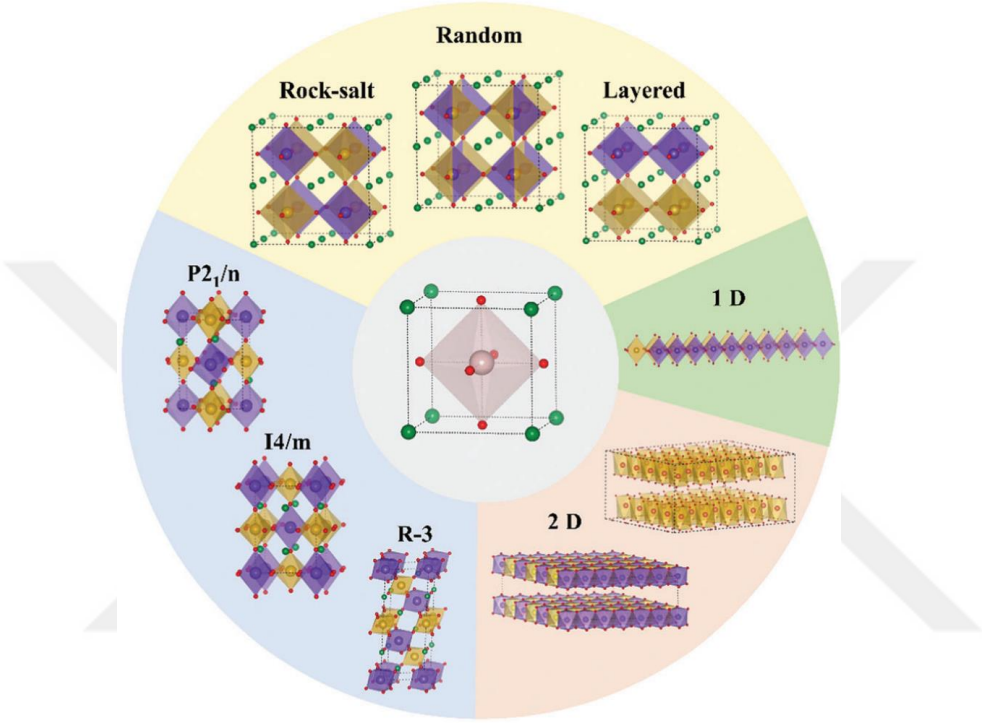

Figure 2.4 The schematic representation of different crystal types of perovskites. Center single perovskite surrounding various crystal structures [36].

The tolerance factor and crystal symmetry are directly proportional to the radius of the A-site cation. La^{3+} tends to form most symmetric phases, such as cubic or rhombohedral. On the other hand, small Pr^{3+} and Nd^{3+} tend to form less symmetric orthorhombic and/or tetragonal phases. Also, large A-site cations, such as Ba^{2+}, distort the symmetry too much and cause the formation of a hexagonal or layered hexagonal crystal structure [36,59,61,63–65,124,145,161]. The electrocatalytic activity is intimately tied to the crystal structure and the configuration of the BO6 octahedral sites. For instance, hexagonal double perovskite oxides feature face-sharing octahedral sites, unlike their cubic counterparts, which predominantly have corner-sharing octahedral configurations.

CHAPTER 3

EXPERIMENTAL PROCEDURE

3.1 Materials

The following chemicals were used as received in this thesis: barium nitrate ($Ba(NO3)_2$, Sigma Aldrich), lanthanum (III) nitrate hexahydrate (La(NO3)3·6H2O, Sigma Aldrich), cobalt(II) nitrate hexahydrate (Co(NO3)2·6H2O, Sigma Aldrich), manganese(II) nitrate tetrahydrate (Mn(NO3)2·4H2O, Sigma Aldrich), Super P carbon (Sigma Aldrich), ethyl alcohol (CH3CH2OH, Sigma Aldrich, 99 %), citric acid (HOC(COOH)(CH2COOH)2, Sigma Aldrich), Nafion solution (Sigma-Aldrich, 5 wt %), carbon cloth (EDTA, Fuel Cell Store), carbon foam (Fuel Cell Store).

3.2 Synthesis of Double Perovskite Oxides

The double perovskite $Ba_xLa_{2-x}CoMnO_{6-\delta}$ (x= 0, 0.5, 1, 1.5, 2) was synthesized using a Pechini method with modifications. Metal nitrates, $Ba(NO_3)_2$, $La(NO_3)_3·6H_2O$, $Co(NO_3)_2·6H_2O$, and $Mn(NO_3)_2·4H_2O$ were dissolved in 100 mL of ultrapure water (18.2 MΩ·cm) in stoichiometric amounts, and stirred continuously. Subsequently, a mixture of citric acid (CA) and acrylamide (AC) was added to the solution as the gelation agent, with a molar ratio of 1:3:9, considering the total metal cation content, CA, and AC, respectively. While incorporating the complexing agents, the solution was stirred at a temperature of 100 °C on a hot plate until a gel-like substance was produced. The gel formation occurs once all physically bonded water has completely evaporated. After evaporation, the gel was subjected to overnight drying at 200 °C under an air atmosphere. This drying step was succeeded by calcination at 600 °C for a duration of 15 hours to eliminate undesired compounds such as H_2O, CO, CO_2,

and NO_2. The powders were subjected to annealing and air-quenching at a temperature of 1300 °C to achieve the formation of the single-phase double perovskite oxide. An example of synthesizing process can be seen in Figure 3.1.

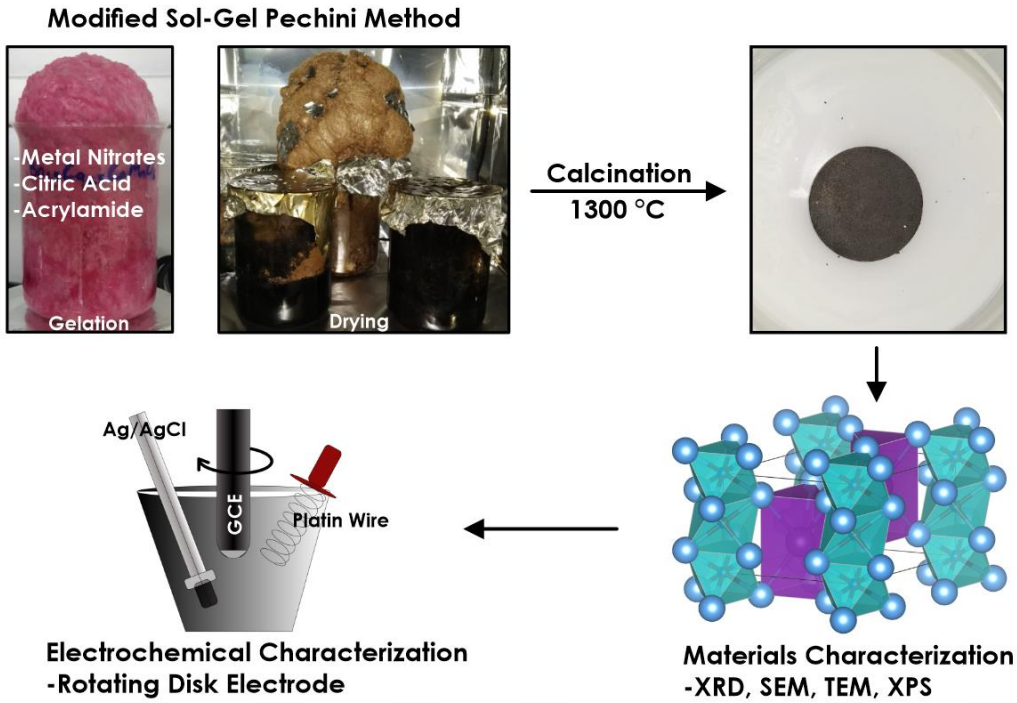

Figure 3.1 The example of the synthesizing procedure from Sol-Gel to the final product.

3.3 Material Characterization

The crystal structure of the synthesized double perovskite oxides was determined using powder X-ray diffraction (XRD) with Cu Kα radiation (λ= 1.5406 Å) in the 2θ range of 20-90 °, employing a Rigaku instrument. The obtained XRD patterns were refined using the Rietveld refinement method through the EXPGUI interface and GSAS software. The morphology and microstructure of the samples were analyzed using a high-resolution field-emission scanning electron microscope (SEM, FEI Nova NanoSEM 430). Additionally, the morphology, microstructure, and crystal structure were characterized using a field-emission high-resolution transmission electron microscope (HRTEM, Tecnai G2 F30). The HRTEM provided high-

resolution and high-angle annular dark-field (HAADF) micrographs, as well as corresponding energy dispersive spectroscopy (EDS) element mapping and selected area electron diffraction (SAED) patterns. The specific areas of the samples were obtained from the Brunauer-Emmet-Teller (BET) method within the P/P_0 = 0.06-0.30 relative pressure rangeX-ray photoelectron spectroscopy (XPS) was performed using the PHI 5000 Versa Probe spectrometer with Al Kα radiation. This technique was employed to investigate the characteristics of the double perovskite oxides, determine their chemical composition, and measure the work function. To ensure accuracy, all peaks were calibrated using a standard C 1s spectrum at 284.6 eV. To measure the work function, approximately 20 nm of Au was sputter-coated onto one half of each specimen. This was done to establish an electrical contact between the sample and the standard sample stage [146]. The samples were placed on a stage for biasing the samples. The stage includes a standard gold foil with a 5.1 eV measured work function value for work function value calibration. The Au work function from the specimen surface was calibrated to the standard Au from the stage. The work function values were calculated from the equation: $\Phi = h\nu - (E_{cutoff} - E_F)$. The "$h\nu$" photon energy is 1486.68 eV. The corrected work function values were obtained using the formula $\Phi_{corrected} = \Phi_{sample} + (\Phi_{stage} - \Phi_{coating})$.

3.4 Electrochemical Characterization

Electrochemical measurements were conducted using a three-electrode rotating disk electrode system (RDE) from BASI, coupled with a GAMRY Reference 3000 potentiostat/galvanostat/ZRA. The three-electrode configuration consisted of an Ag/AgCl reference electrode (immersed in 3 M KCl), a platinum wire counter electrode, and a glassy carbon (GC) working electrode coated with a drop-casted ink of the double perovskite catalyst. The experiments were carried out using a continuous flow of O_2-bubbled and O_2-saturated 0.1 M KOH electrolyte. The preparation of the 0.1 M KOH electrolyte involved dissolving KOH pellets in ultrapure water (with a resistivity of 18.2 MΩ). To account for the electrolyte

resistance, all recorded potentials were iR-corrected. The potentials collected from Ag/AgCl reference electrode were converted to the reversible hydrogen electrode (RHE) according to the Nernst Equation:

$E_{vs.RHE} = E_{vs.Ag/AgCl} + 0.0059 \times pH + 0.1976$ pH for 0.1 M KOH = 12.6 (3.1).

3.4.1 Catalyst Ink Preparation

To assess the activity of the double perovskite oxides in oxygen reactions, the specimens needed to be prepared as working electrodes. For this purpose, a catalyst ink was formulated and deposited onto glassy carbon electrodes (with a diameter of 3 mm). The catalyst ink was created by combining 10 mg of the double perovskite oxide, 5 mg of Super-P carbon, 2 mL of ethanol, and 200 μL of Nafion solution. This mixture was then thoroughly mixed using a mortar and pestle until a homogeneous solution was achieved. Subsequently, the mixture underwent ultrasonication for a minimum of three hours to disperse any agglomerates and maintain uniformity. The fabrication of the working electrode involved depositing 10 μL of the catalyst solution onto the glassy carbon electrode, resulting in a mass loading of 0.557 mg oxide cm^{-2}. Prior to each experiment, the surface of the glassy carbon electrode was polished using a 0.05 μm alumina suspension.

3.4.2 Rotating Disk Electrode (RDE) Experiments

The electrocatalytic performance of the double perovskite oxide materials in OER and ORR was evaluated through experiments utilizing a RDE configuration. A photograph of the RDE set up used in this thesis is shown in Figure 3.2. The RDE setup includes a rotating shaft that constantly stirs the electrolyte solution, allowing a well-defined and homogenous solution flow pattern. Additionally, the rotation of the electrode prevents the accumulation and depletion of reactants at the electrode's tip. In the setup of a RDE, the reaction rate on the electrode surface is primarily governed by kinetics, as the electrode's rotation manages the transfer of reactants.

Reactants reach the electrode surface, and products are carried away. In contrast, under static conditions, the reaction rate on the electrode surface is influenced by both kinetics and mass transport. All experiments with the RDE were conducted in an electrolyte of 0.1 M KOH saturated with O_2, and the rotation speed was set at 1600 rpm, unless specified otherwise.

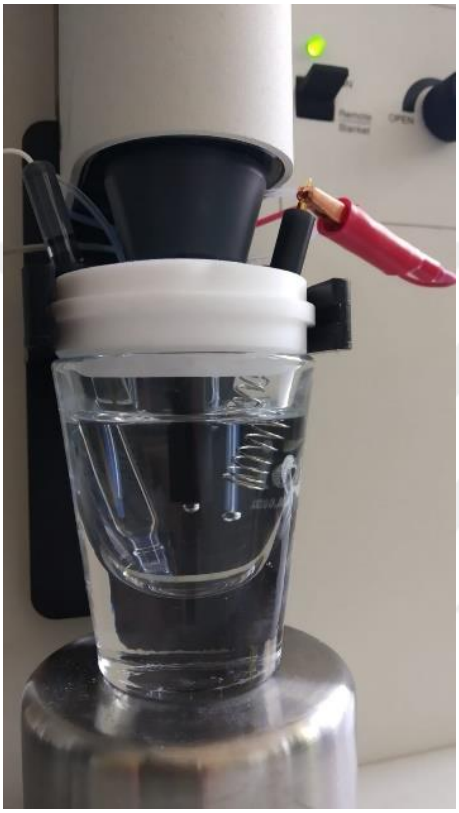

Figure 3.2 The RDE setup used in the experiments.

Prior to each experiment, a series of 10 cyclic voltammetry (CV) cycles were conducted at a scan rate of 100 mV/s. This process aimed to cleanse, activate, and stabilize the surface of the electrocatalyst.

The linear sweep voltammetry (LSV) was conducted to measure the double perovskite oxide electrocatalyst's overpotential and turnover frequency (TOF). In the LSV experiment, the current of the working electrode is determined by the potential difference between the reference and working electrode. The potential is swept linearly over a specified range. For the OER, the LSV measurements were conducted

within the range of 0.2 to 1.1 V vs. Ag/AgCl, while for the ORR, the range was 0.1 to -0.8 V vs. Ag/AgCl. The scan rate for both cases was set to 10 mV/s.

The mass activity (MA) and specific activity (SA) are computed to enhance the comparison of electrocatalysts among themselves and with existing literature, mitigating the impact of mass loading and surface area. These activities are determined using the following equations:

$$MA = J / m \text{ and } SA = J / (10 \times m \times S_{BET}) \quad (3.2)$$

where J, m, and S_{BET} are the current density (mA cm^{-2}), the mass loading (0.557 mg_{oxide} cm^{-2}), and BET surface area (m^2 g^{-1}), respectively.

To explore the kinetics of the double perovskite oxide electrocatalysts, a Tafel analysis was employed under stable conditions. The Tafel analysis was conducted using the chronoamperometry (CA) technique within a potential range of 0.4 – 0.59 V vs. Ag/AgCl, which is in the range of where the OER take place for synthesized perovskite oxides, with voltage increments of 0.01 V. The current at the conclusion of each voltage increment was recorded, and Tafel plots were constructed based on these current and voltage values.

Electrochemical impedance spectroscopy (EIS) was employed to assess the impedance characteristics of the electrocatalysts. EIS measurements were carried out over a frequency range of 0.1 MHz to 0.01 Hz, utilizing a 10 mV AC voltage, and the results were recorded at the voltage of OER start, 0.7 V vs. Ag/AgCl, in a 0.1 M KOH electrolyte.

The long-term durability was evaluated using the chronopotentiometry (CP) technique at a consistent current density of 10 mA cm-2 for a duration exceeding sixty hours. The CP measurements were conducted without the rotation of the working electrode.

To examine the band bending characteristics of the electrocatalyst within the OER potential range, Mott-Schottky (MS) analysis was carried out. This analysis involved performing EIS measurements over a potential range of open circuit voltage (OCP)

-0.5 V to 0.6 V vs. Ag/AgCl in increments of 50 mV. The space charge capacitance was calculated using the following equation:

$$C = -1 / 2\pi v Z'' \quad (3.3)$$

Z" is the imaginary part of the impedance at the constant frequency v = 10 Hz.

3.4.3 Zinc-Air Battery Experiments

The LCM and BCM battery performance was evaluated by assembling a homemade zinc-air battery (Figure 3.3). Anode is a commercial zinc-foil, cathode consists of carbon cloth gas diffusion layer (ELAT), PTFE film, and drop-casted LCM or BCM electrocatalyst, and the electrolyte is 6 M KOH with 0.2 M $Zn(OAc)_2$. The cathode comprises three layers: the outer layer is a PTFE film that prevents electrolyte leakage and facilitates oxygen exchange; the middle layer is a carbon cloth that enables oxygen diffusion and supports the electrocatalyst layer; the inner layer, in contact with the electrolyte, consists of a drop-casted electrocatalyst to facilitate the OER and ORR reactions.

Figure 3.3 Homemade Zinc-Air battery cell.

The assembled Zn-Air battery's performance was tested with GAMRY Interface 1000 potentiostat/galvanostat/ZRA. Charge and discharge polarization curves, along

with the corresponding power densities, were obtained for Zn-air batteries based on both BCM and LCM. These measurements were conducted across a current density range of 0 to 200 mA cm^{-2}. To determine the specific capacities of these Zn-air batteries, they were fully discharged within a current density range of 5 mA cm^{-2} to 50 mA cm^{-2}. Additionally, specific capacities and specific energies were calculated using the provided equations.

$$Specific\ Capacitiy = \frac{I \times t}{m} \tag{3.4}$$

$$Specific\ Energy = \frac{I \times V \times t}{m} \tag{3.5}$$

where I is the applied current density (mA cm^{-2}), t is the total discharge time (hours), m is the consumed mass of the zinc anode (grams), and V is the voltage of the nominal discharge (volts). Following the assessment of specific capacities, the cyclic charge-discharge performance of the Zn-Air batteries was evaluated at a constant current density of 5 mA cm^{-2}. The cycles consisted of 5 minutes of charging followed by 5 minutes of discharging.

CHAPTER 4

RESULTS and DISCUSSION

The oxygen evolution reaction activities of the double perovskite oxide electrocatalysts' series, $Ba_{2-x}La_xCoMnO_{6-\delta}$, were investigated. All synthesized double perovskite oxides were examined, but only the most promising electrocatalyst, $Ba_2CoMnO_{6-\delta}$, was studied in detail. The double perovskite oxides were subjected to structural characterization using techniques such as XRD, SEM, TEM, and BET. The electronic structure was examined through XPS and EPR analyses. Electrochemical evaluation was carried out using a three-electrode system with a rotating disk electrode setup in an O_2-saturated 0.1 M KOH electrolyte. Various parameters including overpotentials under different conditions, Tafel slopes, EIS values, turnover frequencies, Mott-Schottky analysis, work functions, pre- and post-stabilities, as well as battery performance were thoroughly investigated for the double perovskite oxide electrocatalysts.

4.1 Crystal Structure of the Catalysts

Multiple $Ba_2Co_xMn_{2-x}O_{6-\delta}$ samples were synthesized, each having different Co/Mn ratios and being subjected to varying annealing temperatures. This was done to achieve a single-phase crystal structure in the samples. XRD analysis of the samples annealed at 1100 °C reveals the presence of individual perovskite phases, BaCoO3 and BaMnO3, as shown in Figure 4.1(a). This suggests that an annealing temperature of 1100 °C is insufficient to yield a single-phase double perovskite oxide. Therefore, raising the annealing temperature becomes necessary. Subsequent annealing at 1300 °C followed by cooling in the furnace introduces minor oxide phases, as indicated by the XRD pattern in Figure 4.1(b). Therefore, we designed a rapid air-quench method from 1300 °C, and the obtained Ba_2CoMnO_6 (BCM) sample has a 2H

hexagonal perovskite oxide phase without any impurity and secondary phases. On the other hand, $Ba_2Co_{0.5}Mn_{1.5}O_{6-\delta}$ still contains a secondary phase even at this annealing temperature, and $Ba_2Co_{1.5}Mn_{0.5}O_{6-\delta}$ partially melted at 1300 °C, it can be related to Co-rich inter-oxidic phases, the XRD patterns of synthesized $Ba_2Co_xMn_{2-x}O_{6-\delta}$ samples at different chemical compositions and annealing temperature are shown in Figure 4.1(c). Also, as shown in Figure 4.1(d), there is a transformation from multiphase to single phase when the sintering temperature increases for BCM. Consequently, our attention is directed towards the highly electrocatalytically active BCM. In our investigation, we replace trivalent La with divalent Ba at the A-site. This substitution is aimed at comprehending the alterations in crystal and electronic structure, along with their impact on OER performance.

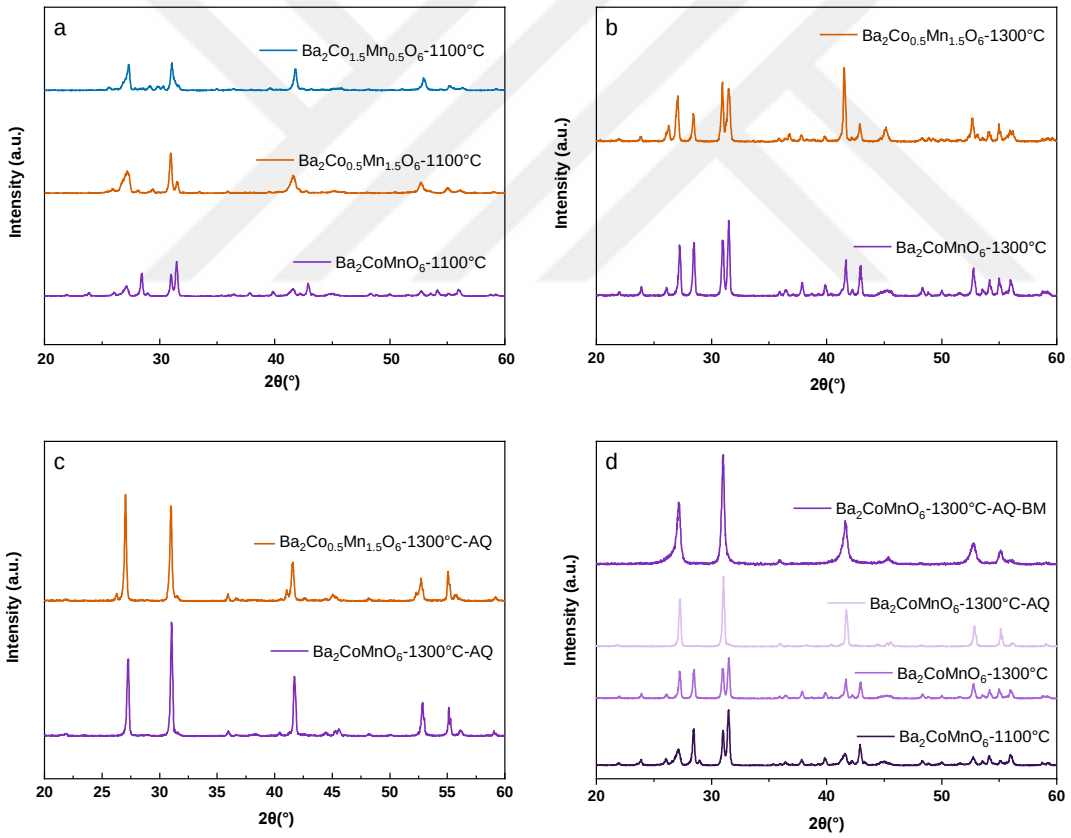

Figure 4.1 The XRD patterns for Ba-Co-Mn-O system (a) at 1100 °C furnace cooled, (b) 1300 °C furnace cooled, (c) 1300 °C air quenched (AQ), and (d) XRD patterns for BCM synthesizing at different temperatures and ball-milled (BM).

The XRD patterns of successfully synthesized single phase 2H hexagonal BCM and its La-containing derivatives, such as cubic $La_2CoMnO_{6-\delta}$ (LCM) and series of $Ba_xLa_{2-x}CoMnO_6$ (x = 0, 0.5, 1, 1.5, 2) are shown in Figure 4.2(a). The 2H-hexagonal crystal structure with *P6₃/mmc* space group (Pearson's Crystal Data: 1900378) of 1300 °C annealed and air-quenched BCM was confirmed by Rietveld refinement analysis, shown in Figure 4.2 (b), (c), (d), (e), (f) for LCM, BLCM-5, BLCM, BLCM-15, and BCM, respectively. The 2H-hexagonal BCM has a = 5.77 Å, c = 4.37 Å lattice constants with the space group *P6₃/mmc*. On the other hand, $La_2CoMnO_{6-\delta}$ exhibits a cubic perovskite structure characterized by the $Fm\bar{3}m$ space group. Similarly, $Ba_{0.5}La_{1.5}CoMnO_{6-\delta}$ (BLCM-5) also manifests a single-phase cubic perovskite structure within the $Fm\bar{3}m$ space group. The crystal structures of both cubic and hexagonal perovskite oxides are depicted in Figure 4.3.

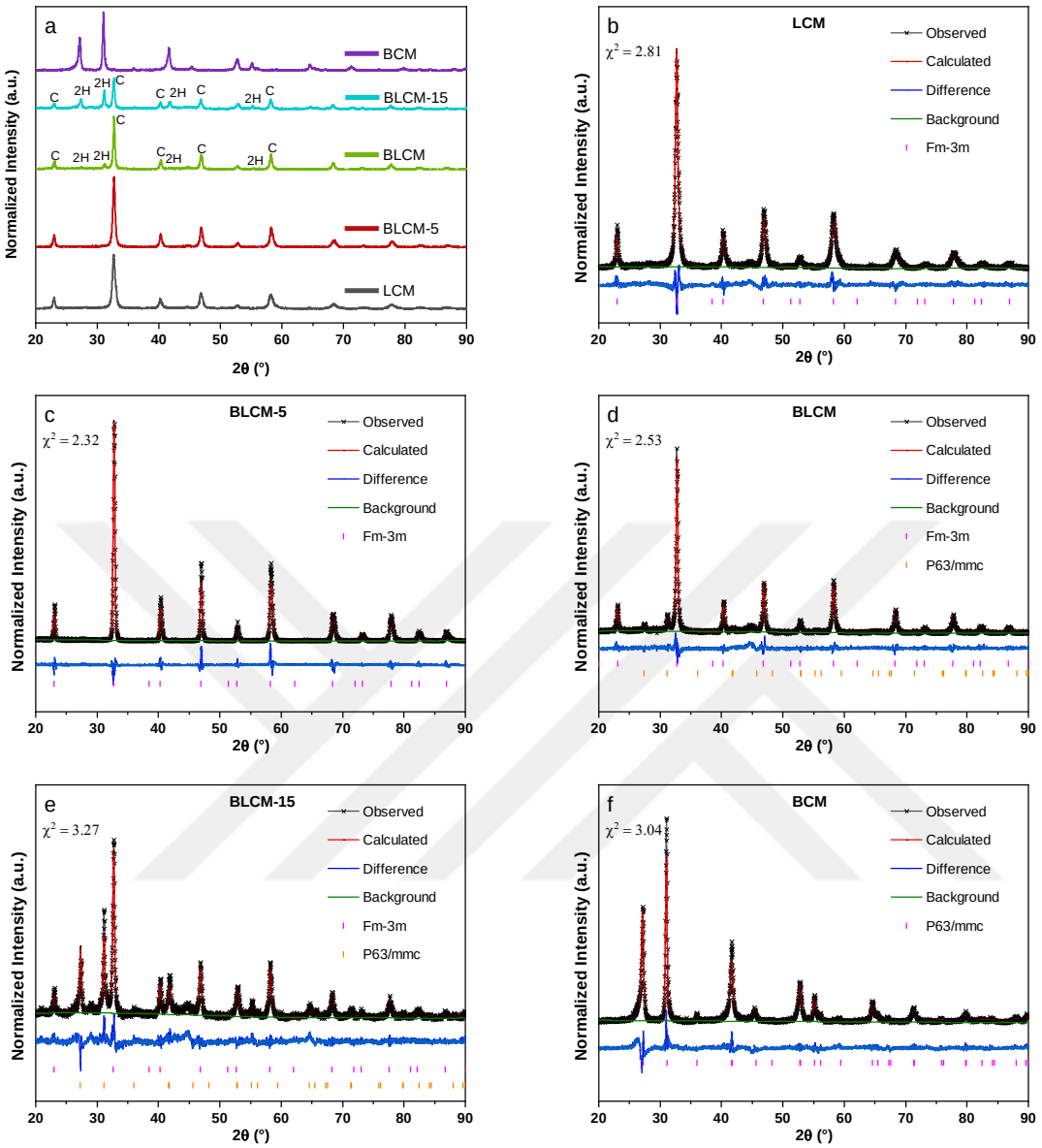

Figure 4.2 (a) XRD patterns of the double perovskite series of $La_2CoMnO_{6-\delta}$ (LCM), $Ba_{1.5}La_{0.5}CoMnO_{6-\delta}$ (BLCM-5), $BaLaCoMnO_{6-\delta}$ (BLCM), $Ba_{0.5}La_{1.5}CoMnO_{6-\delta}$ (BLCM-15), and Ba_2CoMnO_6 (BCM). Rietveld refinement profile of XRD for (b) LCM, (c) BLCM-5, (d) BLCM, (e) BLCM-15, (f) BCM.

The others, $BaLaCoMnO_{6-\delta}$ (BLCM) and $Ba_{1.5}La_{0.5}CoMnO_{6-\delta}$ (BLCM-15) have both 2H-hexagonal perovskite oxide structure and cubic structure. The results show that when the Ba amount increases, the amount of the hexagonal phase increases, and the cubic phase decreases. As a result, if A-site is totally occupied by Ba atoms, the crystal structure is hexagonal; if it is La atoms, the crystal structure turns cubic. The

Rietveld refinement results of the samples, the crystal structure, lattice parameters, also Goldschmidt tolerance factors were summarized in Table 4.1. Goldschmidt tolerance factor gives basic information about the perovskite oxides, such as whether this composition forms a perovskite oxide or what would be the crystal structure. The Goldschmidt tolerance factor equation takes into account the tolerance factor (t_f) along with the average radii of A-site cations (r_A), B-site cations (r_B), and oxygen anions (r_O). In this context, tolerance factor values falling between 0.8 and 1.0 indicate the likelihood of a cubic structure forming, whereas a tolerance factor exceeding 1.0 suggests the potential formation of a hexagonal structure. The XRD findings of the synthesized BCM, LCM, and other materials align well with the predictions derived from the Goldschmidt tolerance factor.

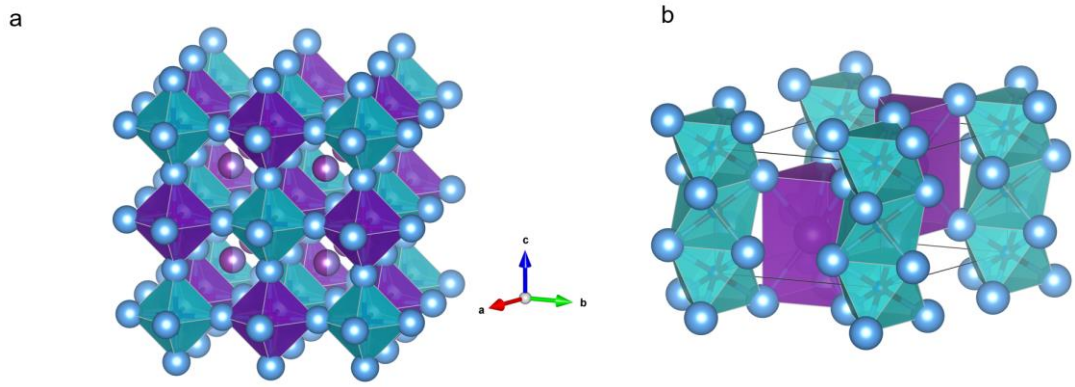

Figure 4.3 Representative crystal structure of (a) cubic $Fm\bar{3}m$ LCM perovskite oxide and (b) 2H-hexagonal $P6_3/mmc$ BCM perovskite oxide.

Table 4.1 Rietveld refinement analysis and Goldschmidt tolerance factor of double perovskite series of $Ba_xLa_{2-x}CoMnO_6$ (x = 0, 0.5, 1, 1.5, 2)

	Lattice Parameter (*Å*)					
Catalyst	**a**	**b**	**c**	**Space Group**	**Volume($Å^3$)**	**Tolerance Factor**
LCM	7.76	7.76	7.76	$Fm\bar{3}m$	466.620	0.991
BLCM-5	7.77	7.77	7.77	$Fm\bar{3}m$	469.097	0.997
BLCM	7.79	7.79	7.79	$Fm\bar{3}m$(90wt%)	472.365	1.023
	5.78	5.78	4.35	$P6_3/mm$(10wt%)	125.706	
BLCM-15	7.79	7.79	7.79	$Fm\bar{3}m$(59wt%)	471.99	1.045
	5.78	5.78	4.35	$P6_3/mmc$(41wt%)	125.810	
BCM	5.77	5.77	4.37	$P6_3/mmc$	126.362	1.063

Additionally, the crystal structure of the 2H-hexagonal BCM was verified through HRTEM and the corresponding SAED techniques. The HRTEM image captured in the [001] projection, as depicted in Figure 4.4(a), illustrates a hexagonal arrangement of atoms. A central atom is surrounded by six others, forming a hexagonal pattern with a measured spacing of d=0.5 nm, corresponding to the (100) lattice planes. Moreover, Figure 4.4(b) displays the corresponding SAED pattern of BCM along the [001] direction. The SAED pattern confirms the hexagonal nature of BCM. The d-spacing determined from the SAED pattern aligns well with the d-spacing obtained from XRD and Rietveld refinement analyses. These findings provide evidence of the successful synthesis and formation of the 2H layered hexagonal perovskite oxide structure in BCM.

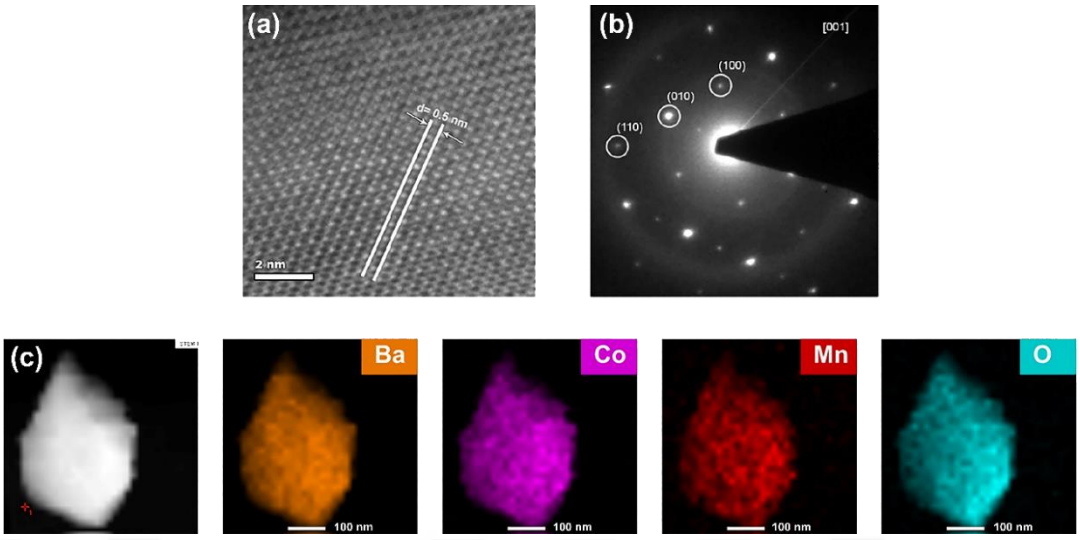

Figure 4.4 (a) HRTEM image of BCM, (b) SAED patterns along the [001] axis for BCM, and (c) HAADF image alongside corresponding EDS element mappings highlighting the presence of Ba, Co, Mn, and O in BCM.

Moreover, the morphological characteristics of the synthesized double perovskite oxides were examined using SEM, as depicted in Figure 4.5. The SEM image reveals particles at the submicron scale, measuring several hundred nanometers in size. Although the particles' shape and size are somewhat unevenly distributed due to the air-quenching and ball milling processes, there is a general consistency in particle size and shape across all perovskite oxides. Hence, it can be inferred that the impact of particle size and morphology on the electrocatalytic activity can be considered negligible. Elemental distribution in the double perovskite oxides was examined through EDX mapping. Additionally, TEM confirmed the EDX mapping results for BCM, as seen in Figure 4.4(c). The outcomes revealed a uniform distribution of all elements—Ba, La, Co, Mn, and O—across the particles. The specific surface area of the particles was determined using N2 adsorption/desorption isotherms and calculated using the Brunauer-Emmet-Teller (BET) method. The BET results, presented in Table 4.2, indicate that the catalysts share a similar specific surface area. Consequently, the influence of surface area on the electrocatalytic activity can be discounted, enabling focused investigation into the impact of elements and doping.

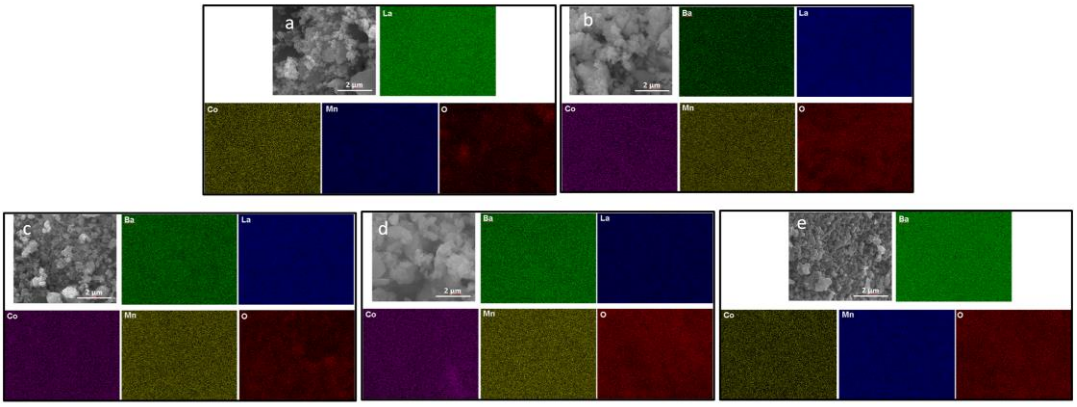

Figure 4.5 SEM images and EDS mapping of the (a) LCM, (b) BLCM-5, (c) BLCM, (d) BLCM-15, (e) BCM.

Table 4.2 BET analysis results

Sample	Multipoint BET				Single Point BET	
	P/P_0	Volume(cc/g)	Slope	Area(m^2/g)	P/P_0	Area(m^2/g)
LCM	0.06112	2.5671	173.9	18.90	0.31144	18.78
	0.08765	2.9831				
	0.11267	3.3101				
	0.16424	3.9766				
BLCM-5	0.06059	2.2213	239.8	13.99	0.31222	14.82
	0.08756	2.5237				
	0.11270	2.7681				
	0.16231	3.2281				
BLCM	0.11260	3.7133	132.2	23.96	0.31212	19.90
	0.16231	4.3159				
	0.21161	5.2742				
	0.26221	6.0080				
BLCM-15	0.08743	3.1955	156.2	20.82	0.31207	18.12
	0.11256	3.5191				
	0.16226	4.0865				
	0.21154	4.9035				
BCM	0.06044	2.7515	160.3	20.49	0.31119	19.41
	0.08751	3.1486				
	0.11227	3.6338				
	0.16214	4.3677				

4.2 Electronic Structure of the Catalysts

XPS was employed to analyze the surface chemical composition and chemical states of Co, Mn, and O. The survey spectra of the $Ba_xLa_{2-x}CoMnO_6$ series (x = 0, 0.5, 1, 1.5, 2) indicated the absence of impurity elements within the structure. The XPS core level spectra of Co 2s, Mn 2p, and O 1s are depicted in Figures 4.6(a), (b), and 4.7, respectively. The O 1s peak was deconvoluted into three regions, as illustrated in Figure 4.7. The fitted peaks centered around 529.5, 531.2, and 532.6 correspond to the typical metal-oxygen bond, a significant number of defect sites with low oxygen coordination in the material, and chemically and physically adsorbed water on the material's surface.

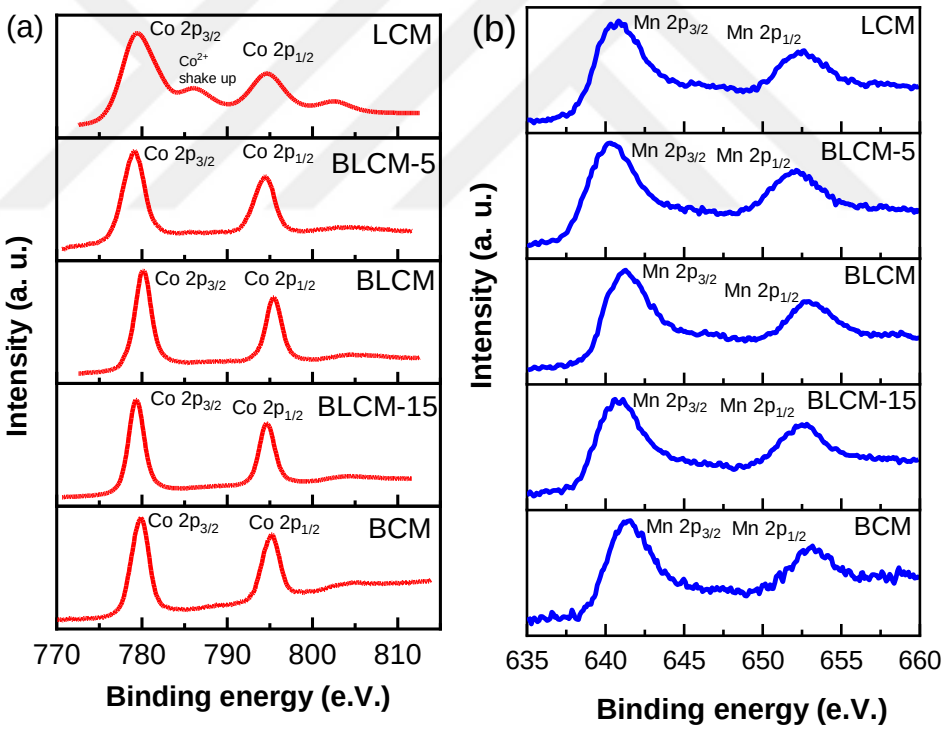

Figure 4.6 XPS core level spectra of (a) Co2p and (b) Mn2p of LCM, BLCM-5, BLCM, BLCM-15, BCM

Comparing all samples, BCM has the strongest metal-oxygen bond indicating more stable oxide formation. In Figure 4.6(a), the XPS core level spectra of Co 2p are depicted. Firstly, the presence of Co^{4+} can be excluded, as the satellite peak with a binding energy of around 789 eV differs from that of Co^{4+} in $SrCoO_3$ [64]. Across all catalysts, the Co 2p spectra exhibit two main peaks along with corresponding weak satellites. The shapes and peak positions (Co $2p_{3/2}$ at around 780 eV and Co $2p_{1/2}$ at around 795 eV) indicate the coexistence of Co^{2+} and Co^{3+}. Differentiation between the oxidation states of Co^{2+} and Co^{3+} is possible by observing the separation in the main peaks and satellites. The main peaks for Co^{2+} are centered at approximately 795 and 780 eV. On the contrary, Co^{3+} exhibits a distinct satellite (Co^{3+} shake-up) at around 789 eV. Additionally, the separation in the main peaks is roughly 6 eV for Co^{2+} and about 9 eV for Co^{3+}. Notably, the Co 2p spectra in Figure 4.6(a) exhibit a strong satellite originating from Co^{2+}, underscoring the predominance of Co^{2+} in the cubic LCM structure [162]. As the Ba content increases, the intensity of the Co^{2+} satellite diminishes, and a weak satellite from Co_3O_4 emerges, accompanied by the formation of the hexagonal phase.

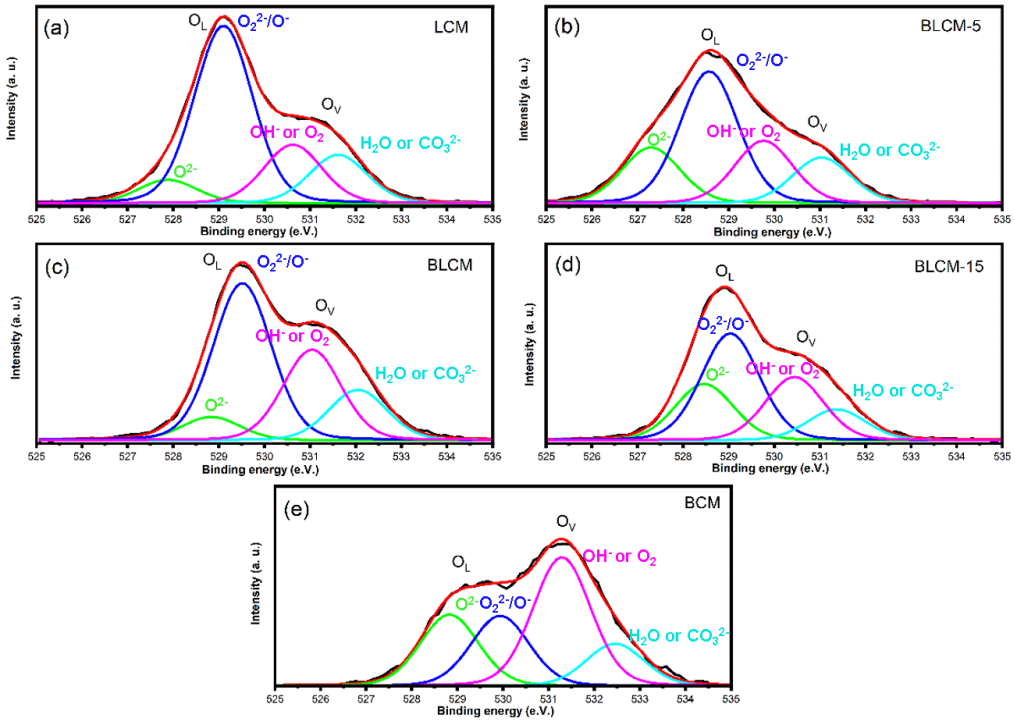

Figure 4.7 XPS core level spectra of (a) LCM, (b) BLCM-5, (c) BLCM, (d) BLCM-15, (e) BCM

According to existing literature, the valence of cobalt in hexagonal perovskite structures is typically higher compared to that in cubic perovskite structures, such as those in the BSCF system. This difference can be attributed to the fact that the distances between B-site cations (B) and oxygen (O) in face-sharing octahedral arrangements are smaller than those in corner-sharing octahedral arrangements. Therefore, the increase in the oxidation of Co through Ba doping is consistent with the literature. Mn 2p core level spectra of the catalysts measured in this work are shown in Figure 4.6(b). Each spectrum exhibits distinct peaks corresponding to Mn $2p_{3/2}$ and $2p_{1/2}$, with a spin-orbit splitting of 11.7 eV. The major peaks, approximately at 640 and 652 eV, can be assigned to Mn $2p_{3/2}$ and Mn $2p_{1/2}$, respectively. By employing peak fitting for Mn $2p_{3/2}$, the spectra provide insights into different valence states of Mn, namely Mn^{4+}, Mn^{3+}, and Mn^{2+}. The specific binding energies associated with these valence states are outlined in Figure 4.6(b). Notably, the observed binding energy of Mn $2p_{3/2}$ closely aligns with those exhibited by MnO_2,

Mn_2O_3, and MnO. Satellites corresponding to the $2p_{3/2}$ and $2p_{1/2}$ peaks are evident within the binding energy range of 646–649 eV and 659–670 eV, respectively. The presence of a satellite at 646 eV signifies the Mn^{2+} oxidation state [17,163]. Moreover, as the content of Ba in the structure increases, this satellite weakens and the Mn $2p_{3/2}$ peak becomes narrower, indicative of an elevated Mn oxidation state, particularly Mn^{+4}. The XPS analysis of the O 1s peak reveals three distinct regions, as depicted in Figure 4.7. The identified peaks at approximately 529.5, 531.2, and 532.6 eV can be attributed to the conventional metal-oxygen bond, a higher concentration of defect sites featuring lower oxygen coordination within the material, and chemically and physically adsorbed water on the material's surface [162]. Notably, the peak associated with oxygen vacancy formation, situated at around ~531 eV, gains prominence in the BCM spectra. This shift indicates that the augmentation of Ba content leads to a more defective oxide crystal structure characterized by an increased presence of oxygen vacancies. This dominant oxygen vacancy peak may be related to the long B-O bond distance in face-sharing octahedral compared to corner-sharing octahedral and short, nearly metallic, B-B bond distance. In a way that supports this, when the amount of hexagonal structure decreases, the intensity of the oxygen vacancy peak decreases, and the lattice oxygen peak increases. The oxygen vacancy of the BCM was also observed via electron paramagnetic spectroscopy (EPR) at a g value of 2.002, Figure 4.8.

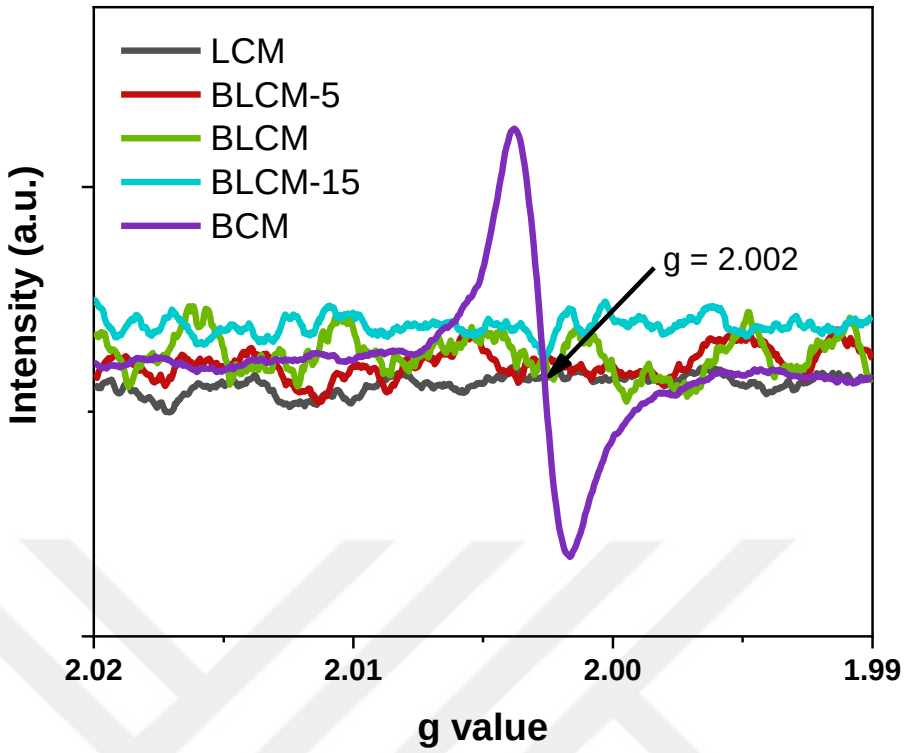

Figure 4.8 Electro paramagnetic resonance (EPR) spectra of $Ba_xLa_{2-x}CoMnO_6$ (x = 0, 0.5, 1, 1.5, 2)

4.3 Electrochemical OER Activity and Stability of the Catalysts

This thesis predominantly centers on investigating the OER performance of BCM and comprehending the factors underlying its heightened activity, given that the OER constitutes a relatively sluggish phase within water-splitting reactions. The research primarily examined a series of double perovskite oxides, denoted as BaxLa2−xCoMnO6 (with varying x values of 0, 0.5, 1, 1.5, and 2), utilizing a three-electrode system with a rotating disk electrode (RDE). The experimental setup consisted of a platinum wire counter electrode, an Ag/AgCl reference electrode, and a glassy carbon (GC) working electrode coated with the double perovskite oxide, with a geometric area of 0.07068 cm^2. The electrolyte is O_2-saturated 0.1 M KOH, and the oxygen gas is continuously purged during the experiment. Before every experiment, cyclic voltammetry (CV) is conducted to clean the surface and activate the electrocatalyst.

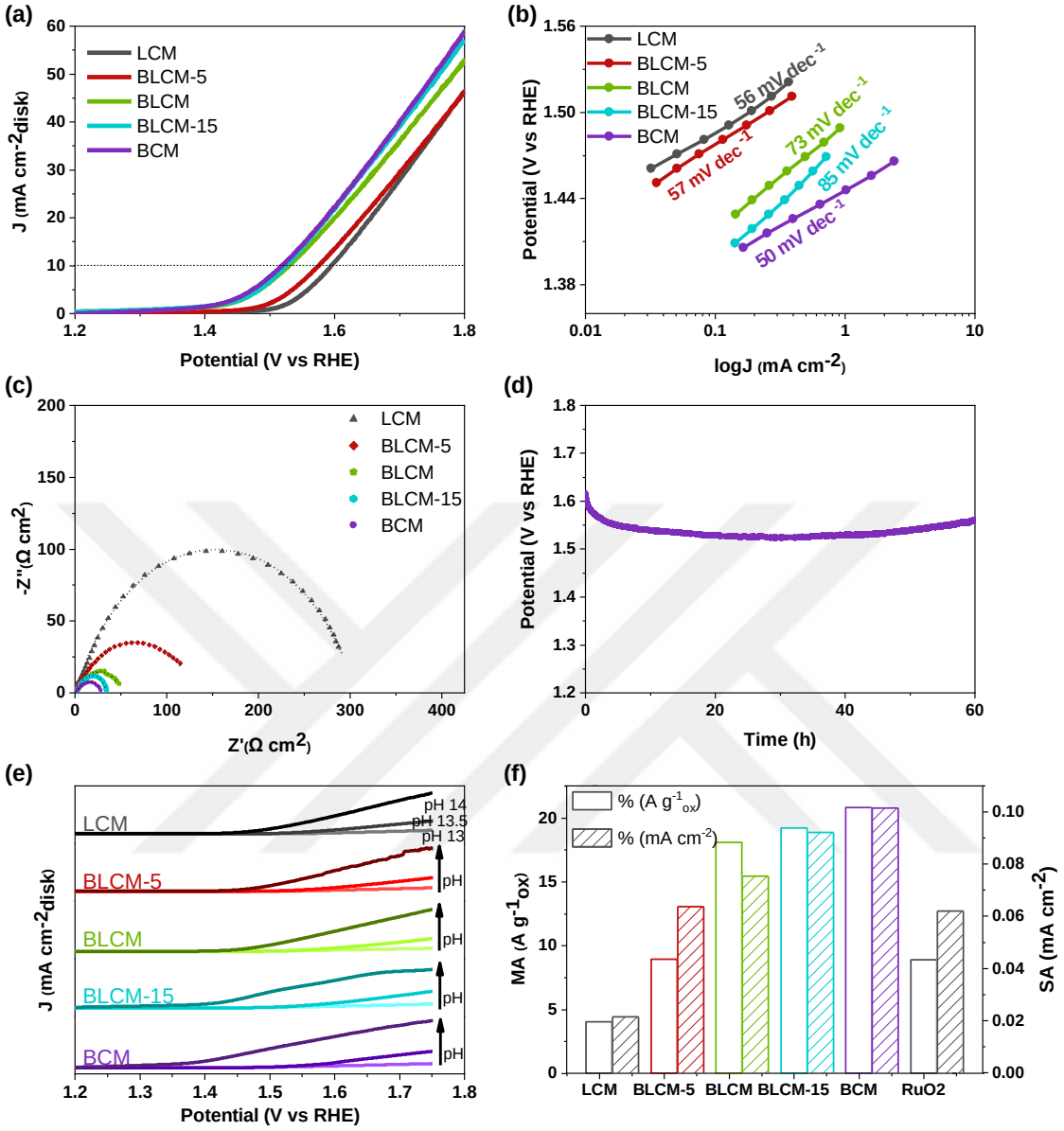

Figure 4.9 (a) LSV curves of double perovskite electrocatalysts at OER region, (b) Tafel plots obtained from steady-state measurements, (c) Chronopotentiometry stability curve of BCM at a current density of 10 mA cm^{-2}, (d) EIS of catalysts, (e) The OER performance at different pH conditions. (f) The specific and mass activity of LCM, BLCM-5, BLCM, BLCM-15, BCM, and RuO_2. RuO_2 data reproduced from Luo, Q.; Lin, D.; Zhan, W.; Zhang, W.; Tang, L.; Luo, J.; Gao, Z.; Jiang, P.; Wang, M.; Hao, L.; Tang, K. Hexagonal Perovskite Ba0.9Sr 0.1Co0.8Fe0.1Ir0.1O3−δ as an Efficient Electrocatalyst towards the Oxygen Evolution Reaction. ACS Appl Energy Mater 2020, 3 (7), 7149–7158. Copyright 2020 American Chemical Society.

To understand the OER performance LSV technique is applied between 0.2 V to 1.8 V. Figure 4.9(a) depicts IR-corrected LSV curves that have been normalized by current density. Notably, an increase in the Ba content within the double perovskite oxide composition leads to a significant reduction in overpotential and a substantial enhancement in OER catalytic activity. The OER activity follows the sequence of BCM > BLCM-15 > BLCM > BLCM-5 > LCM. Notably, BCM consists of solely hexagonal phases, while LCM and BLCM-5 are composed solely of cubic phases. On the other hand, BLCM and BLCM-15 encompass both hexagonal and cubic phases. Incorporating Ba into the composition induces a transition from a cubic to a hexagonal crystal structure, resulting in reduced OER overpotentials. Notably, the hexagonal-containing electrocatalysts, including BLCM (η = 300 mV), BLCM-15 (η = 295 mV), and BCM (η = 288 mV), exhibit significantly lower overpotentials compared to the pure cubic perovskite oxide electrocatalysts: BLCM-5 (η = 346 mV) and LCM (η = 365 mVAdditionally, the electrocatalysts were subjected to testing under higher KOH concentrations, namely 1 M and 6 M. These experiments revealed an enhanced OER performance, yet the catalytic trend remained consistent with the findings from the 0.1 M KOH experiments, as depicted in Figure 4.9(d). These electrochemical results obtained from different pH conditions prove that the synthesized double perovskite oxide electrocatalysts are suitable for various pH applications. In order to gain insights into the fundamental electrochemical kinetics of the samples, Tafel slopes were determined using the multistep chronoamperometry method, with steady-state current variables being taken into consideration. Since the specimen should be in the steady-state current condition to understand the real kinetic behavior, the multistep chronoamperometry method with increasing voltage increments was chosen. This CA test was conducted within the potential range of 1.34 – 1.53 V vs. RHE, with a step increment of 0.01 V, Figure 4.10. This potential range is selected because the water splitting and oxygen evolution reactions take place around these potentials for BCM and other double perovskites. The steady-state current density vs. potential graph is the counterpart of

the LSV curve, and the only difference is the current is measured longer times and reaches steady-state in the multistep CA.

The obtained Tafel slopes from the CA tests are 50, 85, 73, 57, and 56 mV dec-1 for BCM, BLCM-15, BLCM, BLCM-5, and LCM, respectively, as illustrated in Figure 4.9(b). These results highlight the significant impact of the electrocatalyst's single-phase composition and crystal structure on its kinetic behavior.

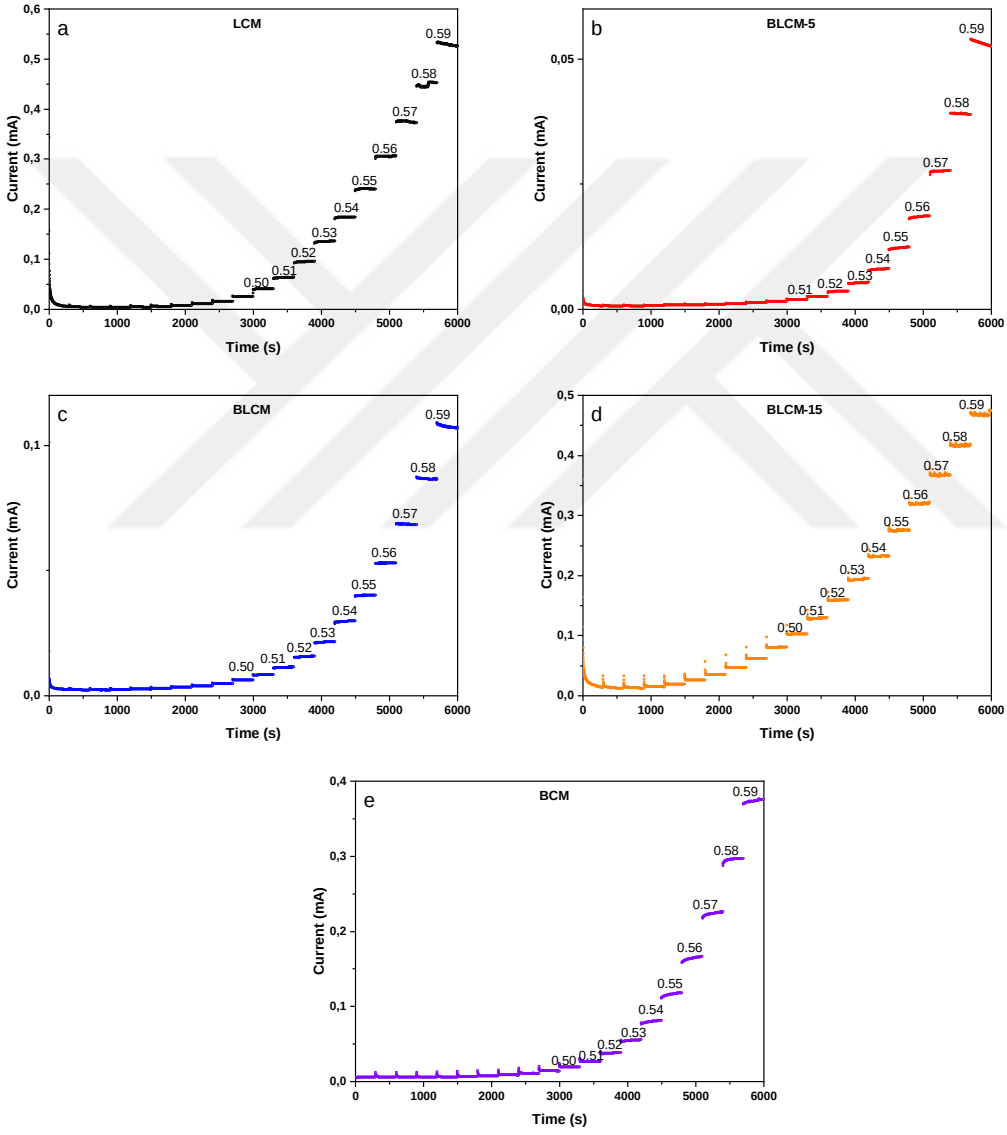

Figure 4.10 Staircase CP to determine the Tafel plot for $Ba_xLa_{2-x}CoMnO_{6-\delta}$ (x = 0, 0.5, 1, 1.5, 2)

Unlike the OER activity and charge-transfer resistance, the barium amount and the hexagonal crystal structure amount are less effective in the kinetics of the electrocatalysts. Kinetics are mainly related to the single-phase and the type of crystal structure. The single-phase LCM and BLCM-5 have a cubic crystal structure, and their Tafel slopes are lower than double-phase BLCM and BLCM-15. Among the synthesized double perovskite oxide electrocatalysts, BCM stands out as the other single-phase electrocatalyst with the highest activity and the most rapid OER kinetics due to its 2H-hexagonal crystal structure. Electrochemical impedance spectroscopy was employed to assess the electrocatalysts' charge-transfer ability and conductivity. The equivalent circuit fitting comprised components such as solution resistance (R_s), a constant-phase element (*CPE*), and charge-transfer resistance (R_{ct}). The charge-transfer resistance of BCM is determined to be 30.86 Ω from the model. This value is notably lower compared to the other synthesized electrocatalysts, namely 306 Ω, 131 Ω, 51 Ω, and 33 Ω for LCM, BLCM-5, BLCM, and BLCM-15, respectively, as depicted in Figure 4.9(c). This reduced charge-transfer resistance in BCM signifies its superior intrinsic electronic conductivity. Additionally, in line with the LSV curves and OER activity, perovskites with hexagonal crystal structures like BCM, BLCM, and BLCM-15 exhibit notably smaller semicircles, indicative of lower resistance, compared to the cubic counterparts, LCM and BLCM-5. The BCM shows great catalytic durability above 60 hours. The catalytic durability of the BCM electrocatalyst was assessed using the chronopotentiometry (CP) method under a constant current density of 10 mA cm^{-2}. The CP measurements revealed that BCM maintains its potential for approximately 60 hours without any significant change, as depicted in Figure 4.9(d). This observation highlights the exceptional stability of BCM, coupled with its outstanding OER activity, surpassing that of existing state-of-the-art catalysts. When evaluating MA and SA, it is notable that perovskite oxides typically exhibit lower values in both parameters. This is primarily attributed to the requirement of high annealing temperatures for achieving a single-phase structure (e.g., above 900 °C). Therefore, to investigate the intrinsic activity of the electrocatalyst, understanding the effect of surface area and mass loading is crucial.

The specific area can be measured with different methods, such as ECSA and BET. In this study, the BET method was conductedThe specific surface area of the electrocatalysts was determined using N_2 adsorption/desorption isotherm curves. The BET results reveal that all the synthesized double perovskite oxides exhibit similar specific surface areas. Consequently, any potential impact associated with specific surface area on the electrocatalytic activity can be disregarded. The uniformity in specific surface areas allows us to isolate and investigate the influence of elements and doping on electrocatalytic effects, making it easier to discern the effects of doping and crystal structure without the interference of other factors. The specific activity is the current density per surface area of the catalyst. The mass activity was also calculated to normalize the catalyst's mass loading during drop-casting. When the Ba amount increases and the hexagonal crystal structure starts to form, both specific activity and mass activity increase sharply, as shown in Figure 4.9(f). The turnover frequency (TOF) is a close approximation to the specific activity. TOF refers to the rate of electron flow through an active site per second, Figure 4.11. Specific activity is a widely used method to determine the intrinsic property of electrocatalysts. TOF is another frequently employed approach for examining intrinsic activity. However, a challenge arises from the often unknown count of active sites. The TOF values demonstrate a notable correlation with the SA graph, and the values are provided along with a comparison to existing literature.

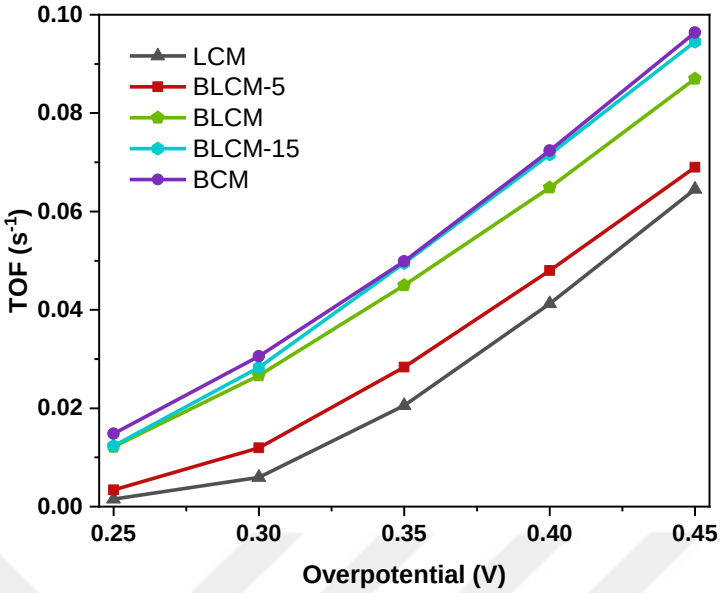

Figure 4.11 TOF values calculated at η = 250, 300, 350, 400, and 450 mV

The investigation of surface work functions and band bending behavior of all catalysts was undertaken to comprehend the underlying factors contributing to the improved electrochemical OER activity of BCM and to identify its OER descriptor. The behavior of band bending at the interface between the solid and liquid phases was explored through MS analysis within the OER potential window. The MS graph is shown in Figure 4.12(a).

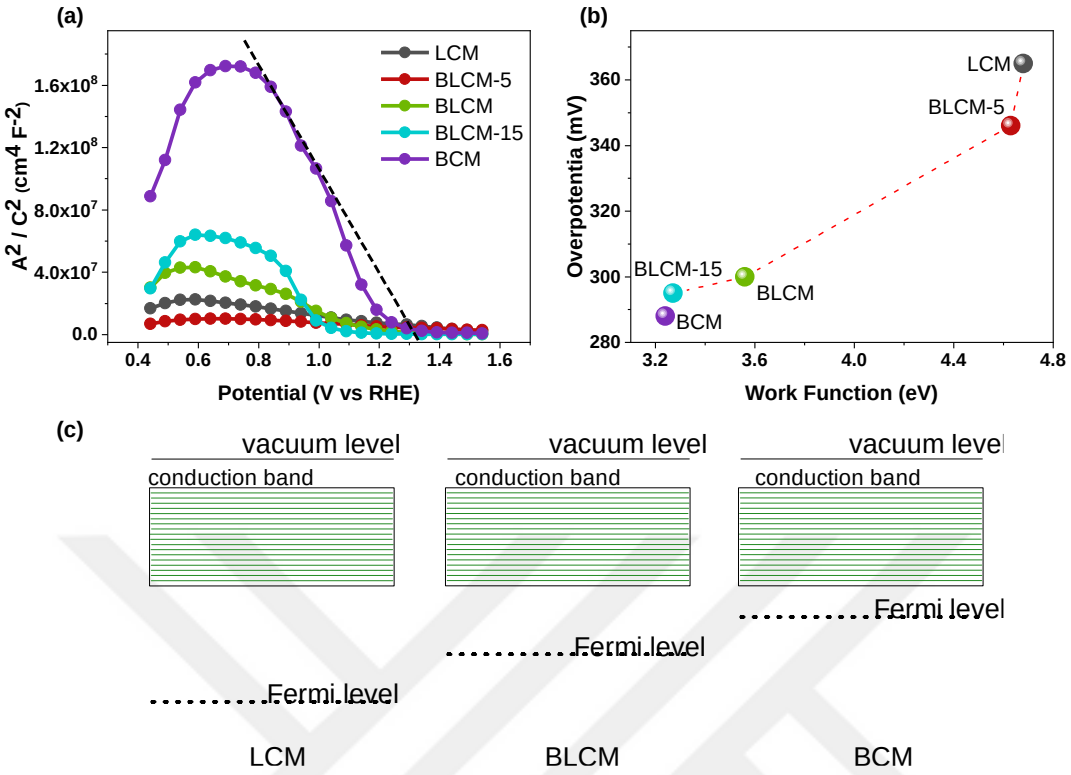

Figure 4.12 (a) Mott-Schottky plots of double perovskite oxide electrocatalyst in alkaline media, (b) Correllation between work function and overpotenial, (c) Reppresentative scheme of Fermi level allignment of LCM, BLCM, and BCM relativve to vacuum.

In all the samples, there is an observable positive slope indicating n-type behavior from the OCV to approximately 0.8 V vs. RHE. This suggests that the surface of the catalyst layers, despite being nominally p-type, experiences charge inversion due to downward band bending. Around the potential of 0.8 V vs. RHE, a transition from n-type (positive slope) to p-type (negative slope) behavior becomes evident. This transition signifies a shift from charge inversion to the hole depletion region [43]. The precise point of transition corresponds to the peak in the Mott-Schottky plots, where the shift from n-type to p-type behavior is identified. The flat-band potential (Efb) is determined by linear extrapolation of the Mott-Schottky plot within the p-type behavior region. The flat-band potential decreases from LCM to BCM. E_{fb} is 1.34 V vs. RHE for BCM and larger than 1.86 V vs. RHE for even BLCM-5. More positive flat-band potential indicates a strong limitation for the OER activity [18,43].

The MS plots exhibit a plateau at the flat-band potential, indicating the occurrence of hole accumulation during the OER process. This flat region signifies the presence of an accumulated positive charge at the interface. For all the samples tested, including LCM, BLCM-5, BLCM, BLCM-15, and BCM, it appears that the OER activity is not primarily governed by electronic charge transfer at the interface.

Indeed, the work function plays a crucial role in influencing the electrocatalyst's performance during the OER process. The work function can be understood as the energy barrier that electrons must overcome to move from the conduction band to the vacuum level. Consequently, a lower work function implies that a greater number of electrons can participate in the reaction, which can have a positive impact on the electrocatalytic activity. The present research delves into the exploration of the work function of the synthesized double perovskite oxides as an experimental approach to uncover any potential correlation with their electrochemical OER activities, as depicted in Figure 4.12(b). The work function assessment is conducted through XPS analysis involving Fermi level and valence band spectral analysis, and further insights can be found in Figure 4.13 and Table 4.3.

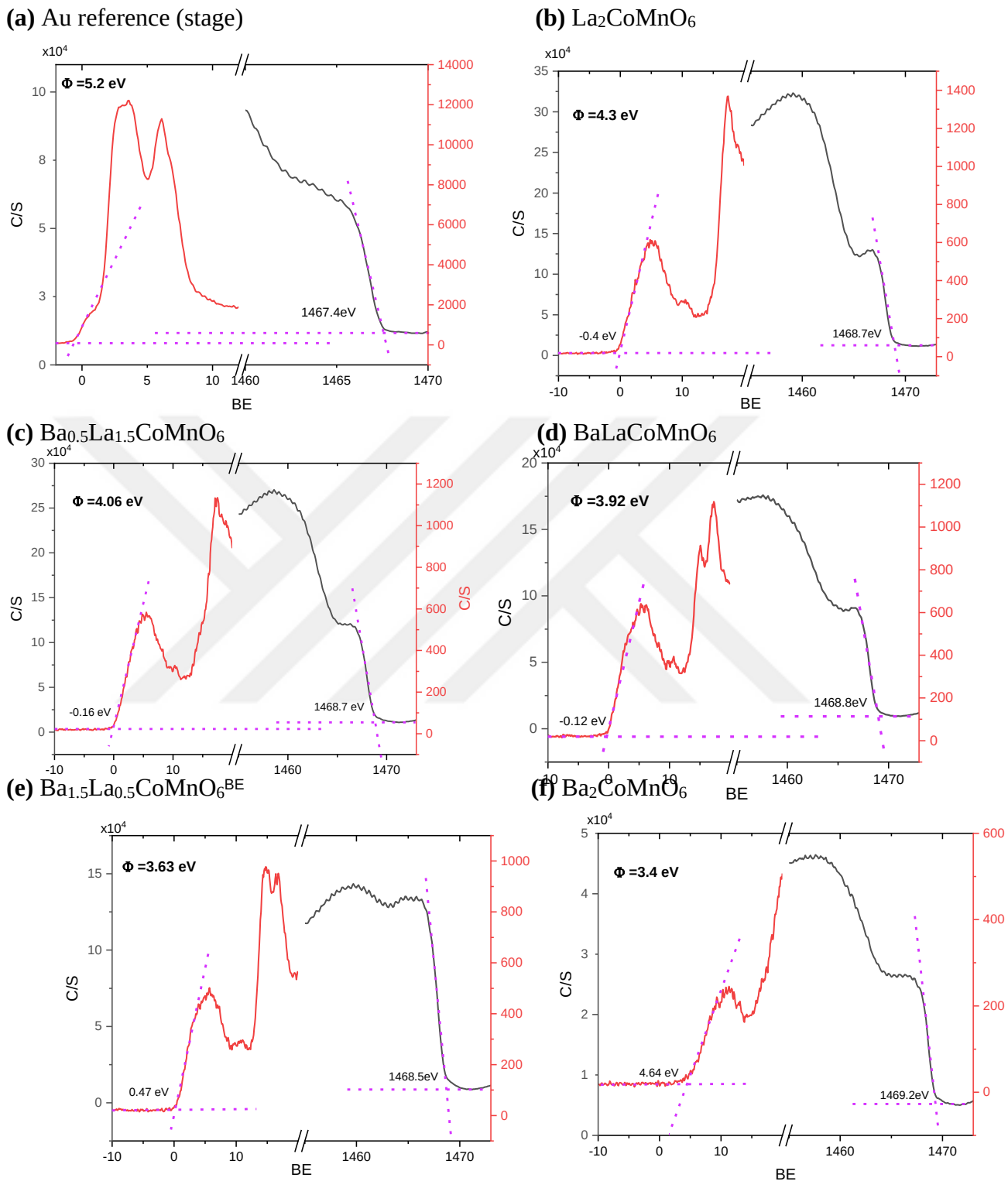

Figure 4.13 Valance and fermi spectra of (a) Au reference, (b) LCM, (c) BLCM-5, (d) BLCM, (e) BLCM-15, (f) BCM.

Nonetheless, it's crucial to emphasize that the measured work functions should be viewed as qualitative trends for the purpose of comparing the tested specimens within this study. As the amount of Ba increases, there is a corresponding decrease in the work function values. This suggests that the intrinsic conductivity of BCM is greater than that of the other samples; this observation is consistent with the findings from EIS measurements. The increase in electronegativity due to the presence of Co and the formation of oxygen vacancies may lead to a modulation of surface electron affinity, in accordance with the Gordy-Thomas relation [18]. Additionally, density functional theory (DFT) calculations and several experimental studies suggest that the reduction in bond distance between B-site elements and the increase in B-O bond distance within face-sharing octahedral sites can provide an explanation for the metallic character of B-B bonds. This metallic bonding characteristic leads to intrinsic metallic conductivity and subsequently lower work function values. As a result, the conclusion can be drawn that BCM, possessing a 2H-hexagonal structure with exclusively face-sharing octahedral sites, exhibits a structural behavior that contributes to its metallic character based on the previous discussion. This structural characteristic likely contributes to the decrease in work function due to the enhanced electronic conductivity.

Table 4.3 Corrected work function values.

	Cut off (BE/eV)	Fermi Level (BE/ev)	ϕ, Work function (eV)	ϕ, Work function (eV)(corrected with Au coating) (eV)
Au coating on LCM	1468.5	-0.79	4.89	*5.2
La_2CoMnO_6(LCM)	1468.7	-0.40	4.37	4.68
Au coating on BLCM-5	1468.7	-0.73	4.63	
$Ba_{0.5}La_{1.5}CoMnO_6$(BLCM-5)	1468.7	-0.16	4.06	4.63
Au coating on BLCM	1468.5	-0.74	4.84	
$BaLaCoMnO_6$(BLCM)	1468.8	-0.12	3.92	3.56
Au coating on BLCM-15	1468.5	-0.74	4.84	
$Ba_{1.5}La_{0.5}CoMnO_6$(BLCM-15)	1468.5	0.47	3.63	3.27
Au coating on BCM	1468.3	-0.74	5.04	
Ba_2CoMnO_6(BCM)	1469.2	4.64	3.40	3.24

The OER electrocatalysts have a trade-off between long-term structural and electrochemical stability. In this study, the BCM electrocatalyst was tested for more than 60 hours in the OER range to observe the electrochemical and structural stability of the electrocatalyst. XPS analysis shows that the oxygen vacancy concentration increases while the chemical state of Co and Mn does not change after sixty hours, Figure 4.14.

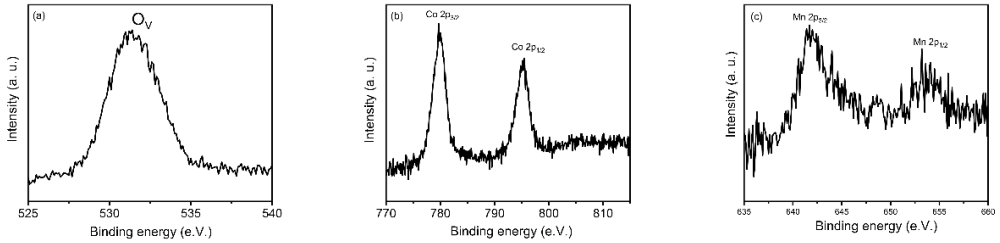

Figure 4.14 XPS core level spectra of BCM after ~ 60 hours of CA test (a) O1s, (b)Co2p and (c)Mn2p

The oxygen vacancies act as active sites; thus, these vacancies can be a source of O_2 production by contributing to charge transport. The long-term stability of BCM at a constant 10 mA cm^{-2} shows that there is a decrease in the nominal voltage and overpotential; this can be related to the increasing metal active sites due to increased oxygen vacancies. Therefore, it can be stated that BCM is very stable under constant current conditions and also exhibits more activation due to newly formed oxygen vacancies. Moreover, BCM is also structurally stable. The TEM images indicate the hexagonal BCM, Figure 4.15. The SAED pattern and the corresponding FFT pattern provide evidence that the structure of BCM remains unchanged even after the sixty-hour duration. The observed results align with the 2H-hexagonal structure observed in the specimen prior to the commencement of the electrochemical test. Notably, no discernible distinction is observed between the structure before the test and the structure following the sixty-hour electrochemical test. In Figure 4.15(b), the HRTEM image highlights the [001] projection, revealing d-spacing values of 2.89 Å for (110) and 2.50 Å for (200) lattice planes. Notably, these d-spacing values align with those documented in Pearson's Crystal Data entry: 1900378. The distribution of

elements in hexagonal BCM is demonstrated through EDX mapping, depicted in Figure 4.15(c). The results indicate a uniform dispersion of Ba, Co, Mn, and O elements across the particle structure. Moreover, the absence of element segregation is evident from the EDX mapping, suggesting that there is no indication of element depletion or segregation even after prolonged service periods. The after-TEM images and after-XPS results provide clear evidence that the 2H hexagonal BCM structure remains stable both during and after the electrochemical tests.

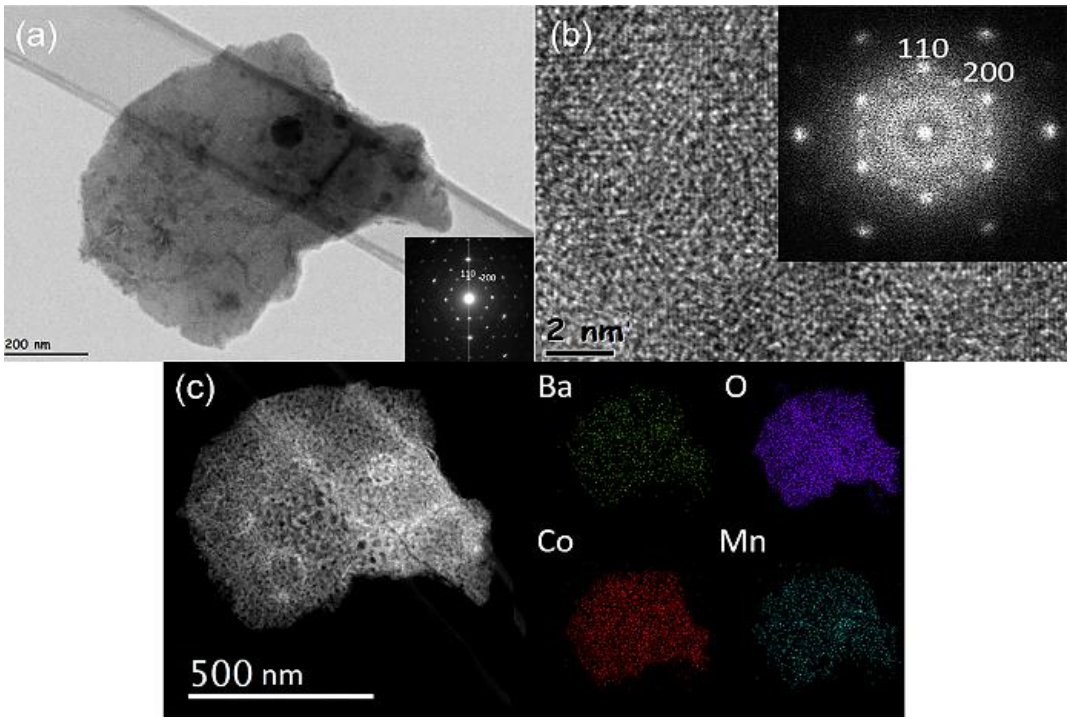

Figure 4.15 After ~ 60 hours of CA test on BCM (a) Bright-field image and SAED pattern (inside) along the [100] axis, (b) HR-TEM image and corresponding FFT pattern (inside) along the [100] axis, (c) HAADF image and corresponding EDS element mapping of Ba, Co, O, and Mn.

4.4 Rechargeable Zinc-Air Battery Performance

The custom-made Zinc-Air battery configuration involves a Zn-foil anode, accompanied by a cathode comprising the double perovskite oxide (LCM or BCM), all operating within a 6 M potassium hydroxide (KOH) electrolyte supplemented with a 0.2 M zinc acetate ($Zn(OAc)_2$) additive. It's important to highlight that during the charging and discharging processes, the surface of the air cathode is where the OER and ORR occur, respectively. The catalytic transformations occurring at the air cathode can be elucidated as follows:

Discharge: $O_2 + 4e^- + 2H_2O \leftrightarrow 4OH^-$ $(E^0 = 0.4\ V)$ *(Oxygen Reduction Reaction)*

Charge: $2OH^- \leftrightarrow \frac{1}{2}O_2 + 2e^- + H_2O$ *(Oxygen Evolution Reaction)*

The open-circuit potential (OCP) of the BCM is 1.652 V, which is higher than the OCP of LCM (1.387 V). As depicted in Figure 4.16(a), the power density of ZABs utilizing LCM and BCM cathodes is presented, along with the corresponding charge and discharge polarization curves. Importantly, the ZAB incorporating a BCM cathode demonstrates a lower charging voltage and a higher discharge voltage compared to the battery using an LCM cathode. This distinct voltage gap serves as an indicator: the ZAB equipped with a BCM cathode presents improved rechargeability owing to the narrower voltage disparity between the OER and ORR. The BCM cathode requires 1.846 V and 1.004 V to reach 10 mA cm^{-2} current density during charge and discharge, respectively. On the other hand, the LCM cathode requires 1.963 V during charging and 0.916 V during discharging. The BCM cathode exhibits 74 mW cm^{-2} peak power density at a high current density of 190 mA cm^{-2}. On the other hand, LCM only has 62 mW cm^{-2} at a comparatively lower curent density of 140 mA cm^{-2}. Figure 4.16(b) illustrates the specific capacities of BCM-based ZABs across various current densities ranging from 5 mA cm^{-2} to 20 mA cm^{-2}, as well as the specific capacity of the LCM-based battery at current densities of 5 mA cm^{-2} and 10 mA cm^{-2}. The BCM-based Zn-air battery at 5 mA cm^{-2} has the highest specific capacity. However, its specific capacity capability at high current

densities is lower than the LCM. Zn-air battery with LCM cathode has near specific capacities at both current densities, but its specific capacities are lower than the BCM-based Zn-air battery.

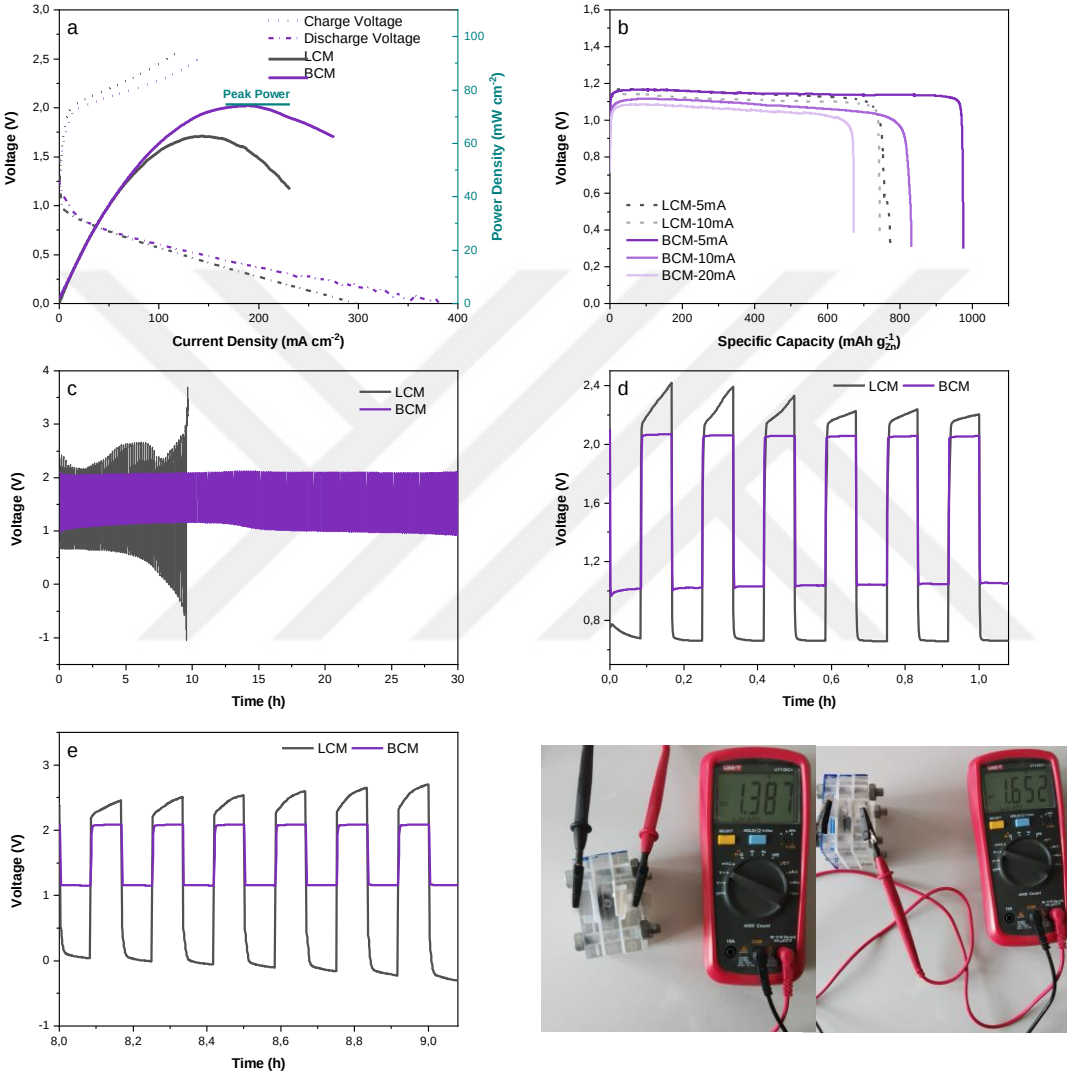

Figure 4.16 Zn-Air batteries with LCM and BCM electrocatalysts as air cathodes' (a) Charge and discharge polarization curves, corresponding peak power density plots, (b) Specific capacities at 5, 10, and 20 mA.cm^{-2} current densities, (c) Cyclic charge-discharge curves at 5 mA.cm^{-2}, (d) Durability performance in the first cycles of cyclic charge-discharge, (d) Durability performance in the last cycles of cyclic charge-discharge, (f, g) Open circuit voltage of LCM and BCM, respectively.

Moreover, the cyclic charge-discharge capacities of the batteries were performed at 5 mA cm^{-2} current density with 10 minutes cycles to understand the electrochemical durability of the double perovskite oxide cathodes. Zn-air battery with BCM cathode shows 2.05 V charge and 1.08 V discharge voltage during cycling with a 0.97 V voltage gap; even after 30 hours of cycling, the voltage gap remains stable, Figure 4.16(c). Therefore, the BCM-based Zn-air battery displays great rechargeability and battery durability. This battery performance indicates that BCM is an efficient catalyst for OER and ORR during charging and discharging for at least 30 hours. On the other hand, the Zn-air battery with LCM cathode exhibits a 2.41 V charge voltage and 0.66 V discharge voltage even at the first cycles. The voltage gap is greater than the BCM-based Zn-air battery, and the differences are clearly seen in Figure 4.16(c), (d). Also, the LCM Zn-air battery lost its stability too early, approximately 10 hours. It indicates that LCM exhibits very low OER/ORR bifunctional electrocatalytic activity and durability. Therefore, the Zn-air battery utilizing the BCM cathode electrocatalyst exhibits superior performance in comparison to the battery employing the LCM cathode. This can be attributed to the enhanced bifunctional activity of BCM, coupled with its robust structural and electrochemical stability. Furthermore, the electrochemical activity of BCM experiences an initial enhancement during the early reaction cycles. This phenomenon can be attributed to the presence of oxygen vacancies, a phenomenon that is further supported by subsequent XPS and EPR analyses.

CHAPTER 5

CONCLUSIONS

In this thesis, novel double perovskite oxide electrocatalysts were synthesized via the air-quenching method. These electrocatalysts were subjected to electrochemical testing for their efficacy in facilitating the oxygen evolution reaction. Furthermore, they were employed in the fabrication of porous air cathodes for utilization in zinc-air batteries.

- We successfully synthesized previously unattainable 2H-$Ba_2CoMnO_{6-\delta}$ through the air-quenching process at extremely elevated temperatures.
- Electrochemical analysis of the OER activity and structural evaluations of $Ba_{2-x}La_xCoMnO_{6-\delta}$ (where x = 0, 0.5, 1, 1.5, 2) reveal that substituting trivalent La with divalent Ba at the A-site triggers the generation of oxygen vacancies, crucial for maintaining charge equilibrium. Consequently, electrocatalysts with elevated Ba content exhibit an increased quantity of oxygen vacancies, effectively creating a surplus of active sites that facilitate the OER process.
- BCM demonstrates a remarkably low overpotential of 288 mV at a current density of 10 mA cm^{-2}, displaying elevated mass and specific activities. Notably, it maintains outstanding electrochemical and structural stability, retaining its 2H-hexagonal crystal structure, Co and Mn element valence and oxidation states, even after 60 hours. Moreover, the overpotential of BCM experiences a slight reduction owing to the emergence of new oxygen vacancies during the operation. The effective OER activity of BCM is closely linked to its structural oxygen vacancy formation and low work function.
- The Zn-air battery featuring the BCM cathode demonstrates exceptionally elevated specific capacities across various current densities, underscoring the substantial activity of BCM during both OER and ORR reactions.

Additionally, this Zn-air battery excels in terms of rechargeability and durability, maintaining a low voltage gap for a minimum of 30 hours. The cyclic charge-discharge performance aligns well with the results from chrono-potentiometric long-term stability assessments.

- The outcomes from this study propose that the A-site management approach holds significant promise in enhancing both the OER activity and structural stability of perovskite oxides. Furthermore, these findings highlight a correlation between the elemental composition, crystal structure, work function, and electrochemical activity of perovskite oxide electrocatalysts, indicating intricate interactions between these factors.

REFERENCES

[1] J. Fu, Z.P. Cano, M.G. Park, A. Yu, M. Fowler, Z. Chen, Electrically Rechargeable Zinc-Air Batteries: Progress, Challenges, and Perspectives, Advanced Materials. 29 (2017) 1604685. https://doi.org/10.1002/adma.201604685.

[2] C. Breyer, A. Gerlach, Global overview on grid-parity, Progress in Photovoltaics: Research and Applications. 21 (2013) 121–136. https://doi.org/10.1002/pip.1254.

[3] L.A.H. Munoz, J.C.C.M. Huijben, B. Verhees, G.P.J. Verbong, The power of grid parity: A discursive approach, Technol Forecast Soc Change. 87 (2014) 179–190. https://doi.org/10.1016/j.techfore.2013.12.012.

[4] R. Li, Y. Li, P. Yang, D. Wang, H. Xu, B. Wang, F. Meng, J. Zhang, M. An, Electrodeposition: Synthesis of advanced transition metal-based catalyst for hydrogen production via electrolysis of water, Journal of Energy Chemistry. 57 (2021) 547–566. https://doi.org/10.1016/j.jechem.2020.08.040.

[5] A.R. Zeradjanin, G. Polymeros, C. Toparli, M. Ledendecker, N. Hodnik, A. Erbe, M. Rohwerder, F. La Mantia, What is the trigger for the hydrogen evolution reaction? – towards electrocatalysis beyond the Sabatier principle, Physical Chemistry Chemical Physics. 22 (2020) 8768–8780. https://doi.org/10.1039/D0CP01108H.

[6] Y. Dai, J. Yu, C. Cheng, P. Tan, M. Ni, Mini-review of perovskite oxides as oxygen electrocatalysts for rechargeable zinc–air batteries, Chemical Engineering Journal. 397 (2020) 125516. https://doi.org/10.1016/j.cej.2020.125516.

[7] Y. Qiu, Z. Liu, Q. Yang, X. Zhang, J. Liu, M. Liu, T. Bi, X. Ji, Atmospheric-Temperature Chain Reaction towards Ultrathin Non-Crystal-

Phase Construction for Highly Efficient Water Splitting, Chemistry – A European Journal. 28 (2022). https://doi.org/10.1002/chem.202200683.

[8] C. Ye, L. Zhang, L. Yue, B. Deng, Y. Cao, Q. Liu, Y. Luo, S. Lu, B. Zheng, X. Sun, A NiCo LDH nanosheet array on graphite felt: an efficient 3D electrocatalyst for the oxygen evolution reaction in alkaline media, Inorg Chem Front. 8 (2021) 3162–3166. https://doi.org/10.1039/D1QI00428J.

[9] Y. Qiu, J. Zhou, Z. Liu, X. Zhang, H. Han, X. Ji, J. Liu, Solar-driven photoelectron injection effect on MgCo2O4@WO3 core–shell heterostructure for efficient overall water splitting, Appl Surf Sci. 578 (2022) 152049. https://doi.org/10.1016/j.apsusc.2021.152049.

[10] H. Sun, X. Xu, H. Kim, W. Jung, W. Zhou, Z. Shao, Electrochemical Water Splitting: Bridging the Gaps Between Fundamental Research and Industrial Applications, ENERGY & ENVIRONMENTAL MATERIALS. (2023). https://doi.org/10.1002/eem2.12441.

[11] X. Zhu, C. Hu, R. Amal, L. Dai, X. Lu, Heteroatom-doped carbon catalysts for zinc–air batteries: progress, mechanism, and opportunities, Energy Environ Sci. 13 (2020) 4536–4563. https://doi.org/10.1039/D0EE02800B.

[12] Y. Li, H. Dai, Recent advances in zinc–air batteries, Chem. Soc. Rev. 43 (2014) 5257–5275. https://doi.org/10.1039/C4CS00015C.

[13] Z. Zhu, Q. Song, B. Xia, L. Jiang, J. Duan, S. Chen, Perovskite Catalysts for Oxygen Evolution and Reduction Reactions in Zinc-Air Batteries, Catalysts. 12 (2022) 1490. https://doi.org/10.3390/catal12121490.

[14] A. Grimaud, O. Diaz-Morales, B. Han, W.T. Hong, Y.-L. Lee, L. Giordano, K.A. Stoerzinger, M.T.M. Koper, Y. Shao-Horn, Activating lattice oxygen redox reactions in metal oxides to catalyse oxygen evolution, Nat Chem. 9 (2017) 457–465. https://doi.org/10.1038/nchem.2695.

[15] N.S. Lewis, D.G. Nocera, Powering the planet: Chemical challenges in solar energy utilization, Proceedings of the National Academy of Sciences. 103 (2006) 15729–15735. https://doi.org/10.1073/pnas.0603395103.

[16] C. Toparli, A. Sarfraz, A.D. Wieck, M. Rohwerder, A. Erbe, In situ and operando observation of surface oxides during oxygen evolution reaction on copper, Electrochim Acta. 236 (2017) 104–115. https://doi.org/10.1016/j.electacta.2017.03.137.

[17] M. Rabe, C. Toparli, Y.-H. Chen, O. Kasian, K.J.J. Mayrhofer, A. Erbe, Alkaline manganese electrochemistry studied by *in situ* and *operando* spectroscopic methods – metal dissolution, oxide formation and oxygen evolution, Physical Chemistry Chemical Physics. 21 (2019) 10457–10469. https://doi.org/10.1039/C9CP00911F.

[18] D. Antipin, M. Risch, Trends of epitaxial perovskite oxide films catalyzing the oxygen evolution reaction in alkaline media, Journal of Physics: Energy. 2 (2020) 032003. https://doi.org/10.1088/2515-7655/ab812f.

[19] H. Han, Y. Qiu, H. Zhang, T. Bi, Q. Yang, M. Liu, J. Zhou, X. Ji, Lattice-disorder layer generation from liquid processing at room temperature with boosted nanointerface exposure toward water splitting, Sustain Energy Fuels. 6 (2022) 3008–3013. https://doi.org/10.1039/D2SE00474G.

[20] Y. Qiu, Z. Liu, X. Zhang, A. Sun, X. Ji, J. Liu, Controllable atom implantation for achieving Coulomb-force unbalance toward lattice distortion and vacancy construction for accelerated water splitting, J Colloid Interface Sci. 610 (2022) 194–201. https://doi.org/10.1016/j.jcis.2021.12.029.

[21] J. Yang, W. Li, K. Xu, S. Tan, D. Wang, Y. Li, Regulating the Tip Effect on Single-Atom and Cluster Catalysts: Forming Reversible Oxygen Species with High Efficiency in Chlorine Evolution Reaction, Angewandte Chemie. 134 (2022). https://doi.org/10.1002/ange.202200366.

[22] S. Cherevko, S. Geiger, O. Kasian, N. Kulyk, J.-P. Grote, A. Savan, B.R. Shrestha, S. Merzlikin, B. Breitbach, A. Ludwig, K.J.J. Mayrhofer, Oxygen and hydrogen evolution reactions on Ru, RuO 2 , Ir, and IrO 2 thin film electrodes in acidic and alkaline electrolytes: A comparative study on activity and stability, Catal Today. 262 (2016) 170–180. https://doi.org/10.1016/j.cattod.2015.08.014.

[23] L. Zhang, J. Wang, P. Liu, J. Liang, Y. Luo, G. Cui, B. Tang, Q. Liu, X. Yan, H. Hao, M. Liu, R. Gao, X. Sun, Ni(OH)2 nanoparticles encapsulated in conductive nanowire array for high-performance alkaline seawater oxidation, Nano Res. 15 (2022) 6084–6090. https://doi.org/10.1007/s12274-022-4391-6.

[24] H. Sun, X. Xu, Y. Song, W. Zhou, Z. Shao, Designing High-Valence Metal Sites for Electrochemical Water Splitting, Adv Funct Mater. 31 (2021) 2009779. https://doi.org/10.1002/adfm.202009779.

[25] Y. Lee, J. Suntivich, K.J. May, E.E. Perry, Y. Shao-Horn, Synthesis and Activities of Rutile IrO_2 and RuO_2 Nanoparticles for Oxygen Evolution in Acid and Alkaline Solutions, J Phys Chem Lett. 3 (2012) 399–404. https://doi.org/10.1021/jz2016507.

[26] A. Karmakar, K. Karthick, S. Kumaravel, S.S. Sankar, S. Kundu, Enabling and Inducing Oxygen Vacancies in Cobalt Iron Layer Double Hydroxide via Selenization as Precatalysts for Electrocatalytic Hydrogen and Oxygen Evolution Reactions, Inorg Chem. 60 (2021) 2023–2036. https://doi.org/10.1021/acs.inorgchem.0c03514.

[27] K. Kannimuthu, K. Sangeetha, S. Sam Sankar, A. Karmakar, R. Madhu, S. Kundu, Investigation on nanostructured Cu-based electrocatalysts for improvising water splitting: a review, Inorg Chem Front. 8 (2021) 234–272. https://doi.org/10.1039/D0QI01060J.

[28] A. Karmakar, K. Karthick, S.S. Sankar, S. Kumaravel, R. Madhu, S. Kundu, A vast exploration of improvising synthetic strategies for enhancing the OER kinetics of LDH structures: a review, J Mater Chem A Mater. 9 (2021) 1314–1352. https://doi.org/10.1039/D0TA09788H.

[29] A. Karmakar, K. Karthick, S.S. Sankar, S. Kumaravel, M. Ragunath, S. Kundu, Oxygen vacancy enriched $NiMoO_4$ nanorods *via* microwave heating: a promising highly stable electrocatalyst for total water splitting, J Mater Chem A Mater. 9 (2021) 11691–11704. https://doi.org/10.1039/D1TA02165F.

[30] S.S. Selvasundarasekar, T.K. Bijoy, S. Kumaravel, A. Karmakar, R. Madhu, K. Bera, S. Nagappan, H.N. Dhandapani, S.-C. Lee, S. Kundu, Constructing electrospun spinel $NiFe_2O_4$ nanofibers decorated with palladium ions as nanosheets heterostructure: boosting electrocatalytic activity of HER in alkaline water electrolysis, Nanoscale. 14 (2022) 10360–10374. https://doi.org/10.1039/D2NR02203F.

[31] R. Madhu, A. Karmakar, S. Kumaravel, S.S. Sankar, K. Bera, S. Nagappan, H.N. Dhandapani, S. Kundu, Revealing the pH-Universal Electrocatalytic Activity of Co-Doped RuO_2 toward the Water Oxidation Reaction, ACS Appl Mater Interfaces. 14 (2022) 1077–1091. https://doi.org/10.1021/acsami.1c20752.

[32] D. Liu, P. Zhou, H. Bai, H. Ai, X. Du, M. Chen, D. Liu, W.F. Ip, K.H. Lo, C.T. Kwok, S. Chen, S. Wang, G. Xing, X. Wang, H. Pan, Development of Perovskite Oxide-Based Electrocatalysts for Oxygen Evolution Reaction, Small. 17 (2021) 2101605. https://doi.org/10.1002/smll.202101605.

[33] H. Wang, M. Zhou, P. Choudhury, H. Luo, Perovskite oxides as bifunctional oxygen electrocatalysts for oxygen evolution/reduction reactions – A mini review, Appl Mater Today. 16 (2019) 56–71. https://doi.org/10.1016/j.apmt.2019.05.004.

[34] J. Hwang, R.R. Rao, L. Giordano, Y. Katayama, Y. Yu, Y. Shao-Horn, Perovskites in catalysis and electrocatalysis, Science (1979). 358 (2017) 751–756. https://doi.org/10.1126/science.aam7092.

[35] X. Cheng, E. Fabbri, M. Nachtegaal, I.E. Castelli, M. El Kazzi, R. Haumont, N. Marzari, T.J. Schmidt, Oxygen Evolution Reaction on $La_{1-x}Sr_xCoO_3$ Perovskites: A Combined Experimental and Theoretical Study of Their Structural, Electronic, and Electrochemical Properties, Chemistry of Materials. 27 (2015) 7662–7672. https://doi.org/10.1021/acs.chemmater.5b03138.

[36] W.-J. Yin, B. Weng, J. Ge, Q. Sun, Z. Li, Y. Yan, Oxide perovskites, double perovskites and derivatives for electrocatalysis, photocatalysis, and photovoltaics, Energy Environ Sci. 12 (2019) 442–462. https://doi.org/10.1039/C8EE01574K.

[37] J. Suntivich, K.J. May, H.A. Gasteiger, J.B. Goodenough, Y. Shao-Horn, A Perovskite Oxide Optimized for Oxygen Evolution Catalysis from Molecular Orbital Principles, Science (1979). 334 (2011) 1383–1385. https://doi.org/10.1126/science.1212858.

[38] K.J. May, C.E. Carlton, K.A. Stoerzinger, M. Risch, J. Suntivich, Y.-L. Lee, A. Grimaud, Y. Shao-Horn, Influence of Oxygen Evolution during Water Oxidation on the Surface of Perovskite Oxide Catalysts, J Phys Chem Lett. 3 (2012) 3264–3270. https://doi.org/10.1021/jz301414z.

[39] I. Yamada, A. Takamatsu, K. Asai, T. Shirakawa, H. Ohzuku, A. Seno, T. Uchimura, H. Fujii, S. Kawaguchi, K. Wada, H. Ikeno, S. Yagi, Systematic Study of Descriptors for Oxygen Evolution Reaction Catalysis in Perovskite Oxides, The Journal of Physical Chemistry C. 122 (2018) 27885–27892. https://doi.org/10.1021/acs.jpcc.8b09287.

[40] H. Sun, S. Song, X. Xu, J. Dai, J. Yu, W. Zhou, Z. Shao, W. Jung, Recent Progress on Structurally Ordered Materials for Electrocatalysis, Adv Energy Mater. 11 (2021) 2101937. https://doi.org/10.1002/aenm.202101937.

[41] Z. Xu, X. Men, Y. Shan, F. Liu, R. Xu, Y. Wang, Y. Shao, Y. Zhu, L. Liu, Electronic reconfiguration induced by neighboring exchange interaction at double perovskite oxide interface for highly efficient oxygen evolution reaction, Chemical Engineering Journal. 432 (2022) 134330. https://doi.org/10.1016/j.cej.2021.134330.

[42] A. Badreldin, A.E. Abusrafa, A. Abdel-Wahab, Oxygen-deficient perovskites for oxygen evolution reaction in alkaline media: a review, Emergent Mater. 3 (2020) 567–590. https://doi.org/10.1007/s42247-020-00123-z.

[43] L. Heymann, M.L. Weber, M. Wohlgemuth, M. Risch, R. Dittmann, C. Baeumer, F. Gunkel, Separating the Effects of Band Bending and Covalency in Hybrid Perovskite Oxide Electrocatalyst Bilayers for Water Electrolysis, ACS Appl Mater Interfaces. 14 (2022) 14129–14136. https://doi.org/10.1021/acsami.1c20337.

[44] J. Xiong, H. Zhong, J. Li, X. Zhang, J. Shi, W. Cai, K. Qu, C. Zhu, Z. Yang, S.P. Beckman, H. Cheng, Engineering highly active oxygen sites in perovskite oxides for stable and efficient oxygen evolution, Appl Catal B. 256 (2019) 117817. https://doi.org/10.1016/j.apcatb.2019.117817.

[45] Y. Duan, S. Sun, S. Xi, X. Ren, Y. Zhou, G. Zhang, H. Yang, Y. Du, Z.J. Xu, Tailoring the Co 3d-O 2p Covalency in $LaCoO_3$ by Fe Substitution To Promote Oxygen Evolution Reaction, Chemistry of Materials. 29 (2017) 10534–10541. https://doi.org/10.1021/acs.chemmater.7b04534.

[46] B.-J. Kim, E. Fabbri, D.F. Abbott, X. Cheng, A.H. Clark, M. Nachtegaal, M. Borlaf, I.E. Castelli, T. Graule, T.J. Schmidt, Functional Role of Fe-Doping in Co-Based Perovskite Oxide Catalysts for Oxygen Evolution Reaction, J

Am Chem Soc. 141 (2019) 5231–5240. https://doi.org/10.1021/jacs.8b12101.

[47] Y. Liu, C. Ye, S.-N. Zhao, Y. Wu, C. Liu, J. Huang, L. Xue, J. Sun, W. Zhang, X. Wang, P. Xiong, J. Zhu, A dual-site doping strategy for developing efficient perovskite oxide electrocatalysts towards oxygen evolution reaction, Nano Energy. 99 (2022) 107344. https://doi.org/10.1016/j.nanoen.2022.107344.

[48] J. Wang, C. Liu, S. Li, Y. Li, Q. Zhang, Q. Peng, J.S. Tse, Z. Wu, Advanced electrocatalysts with Dual-metal doped carbon Materials: Achievements and challenges, Chemical Engineering Journal. 428 (2022) 132558. https://doi.org/10.1016/j.cej.2021.132558.

[49] L. Fan, E.L. Rautama, J. Lindén, J. Sainio, H. Jiang, O. Sorsa, N. Han, C. Flox, Y. Zhao, Y. Li, T. Kallio, Two orders of magnitude enhancement in oxygen evolution reactivity of La0.7Sr0.3Fe1−Ni O3− by improving the electrical conductivity, Nano Energy. 93 (2022) 106794. https://doi.org/10.1016/j.nanoen.2021.106794.

[50] D. Guan, J. Zhong, H. Xu, Y.-C. Huang, Z. Hu, B. Chen, Y. Zhang, M. Ni, X. Xu, W. Zhou, Z. Shao, A universal chemical-induced tensile strain tuning strategy to boost oxygen-evolving electrocatalysis on perovskite oxides, Appl Phys Rev. 9 (2022) 011422. https://doi.org/10.1063/5.0083059.

[51] C. Liu, D. Ji, H. Shi, Z. Wu, H. Huang, Z. Kang, Z. Chen, An A-site management and oxygen-deficient regulation strategy with a perovskite oxide electrocatalyst for the oxygen evolution reaction, J Mater Chem A Mater. 10 (2022) 1336–1342. https://doi.org/10.1039/D1TA09306A.

[52] Y. Zhu, W. Zhou, J. Yu, Y. Chen, M. Liu, Z. Shao, Enhancing Electrocatalytic Activity of Perovskite Oxides by Tuning Cation Deficiency for Oxygen Reduction and Evolution Reactions, Chemistry of Materials. 28 (2016) 1691–1697. https://doi.org/10.1021/acs.chemmater.5b04457.

[53] Y. Sun, R. Li, X. Chen, J. Wu, Y. Xie, X. Wang, K. Ma, L. Wang, Z. Zhang, Q. Liao, Z. Kang, Y. Zhang, A-Site Management Prompts the Dynamic Reconstructed Active Phase of Perovskite Oxide OER Catalysts, Adv Energy Mater. 11 (2021) 2003755. https://doi.org/10.1002/aenm.202003755.

[54] J.T. Mefford, X. Rong, A.M. Abakumov, W.G. Hardin, S. Dai, A.M. Kolpak, K.P. Johnston, K.J. Stevenson, Water electrolysis on La1−xSrxCoO3−δ perovskite electrocatalysts, Nat Commun. 7 (2016) 11053. https://doi.org/10.1038/ncomms11053.

[55] M. Qu, X. Ding, Z. Shen, M. Cui, F.E. Oropeza, G. Gorni, V.A. de la Peña O'Shea, W. Li, D.-C. Qi, K.H.L. Zhang, Tailoring the Electronic Structures of the La_2NiMnO_6 Double Perovskite as Efficient Bifunctional Oxygen Electrocatalysis, Chemistry of Materials. 33 (2021) 2062–2071. https://doi.org/10.1021/acs.chemmater.0c04527.

[56] X. Cao, X. Yan, L. Ke, K. Zhao, N. Yan, Proton-Assisted Reconstruction of Perovskite Oxides: Toward Improved Electrocatalytic Activity, ACS Appl Mater Interfaces. 13 (2021) 22009–22016. https://doi.org/10.1021/acsami.1c03276.

[57] A. Boucly, E. Fabbri, L. Artiglia, X. Cheng, D. Pergolesi, M. Ammann, T.J. Schmidt, Surface Segregation Acts as Surface Engineering for the Oxygen Evolution Reaction on Perovskite Oxides in Alkaline Media, Chemistry of Materials. 32 (2020) 5256–5263. https://doi.org/10.1021/acs.chemmater.0c01396.

[58] A. Boucly, L. Artiglia, E. Fabbri, D. Palagin, D. Aegerter, D. Pergolesi, Z. Novotny, N. Comini, J.T. Diulus, T. Huthwelker, M. Ammann, T.J. Schmidt, Direct evidence of cobalt oxyhydroxide formation on a $La_{0.2}Sr_{0.8}CoO_3$ perovskite water splitting catalyst, J Mater Chem A Mater. 10 (2022) 2434–2444. https://doi.org/10.1039/D1TA04957G.

[59] X. Xu, C. Su, Z. Shao, Fundamental Understanding and Application of $Ba_{0.5}Sr_{0.5}Co_{0.8}Fe_{0.2}O_{3-\delta}$ Perovskite in Energy Storage and Conversion: Past, Present, and Future, Energy & Fuels. 35 (2021) 13585–13609. https://doi.org/10.1021/acs.energyfuels.1c02111.

[60] L. Wei, J. Hu, H. Liu, W. Zhang, H. Zheng, S. Wu, K. Tang, Hexagonal perovskite $Sr_6(Co_{0.8}Fe_{0.2})_5O_{15}$ as an efficient electrocatalyst towards the oxygen evolution reaction, Dalton Transactions. 51 (2022) 7100–7108. https://doi.org/10.1039/D2DT00706A.

[61] L. Tang, W. Zhang, D. Lin, Y. Ren, H. Zheng, Q. Luo, L. Wei, H. Liu, J. Chen, K. Tang, The hexagonal perovskite $Ba_{0.5}Sr_{0.5}Co_{0.8}Fe_{0.2}O_{3-\delta}$ as an efficient electrocatalyst for the oxygen evolution reaction, Inorg Chem Front. 7 (2020) 4488–4497. https://doi.org/10.1039/D0QI00754D.

[62] K.E. Stitzer, J. Darriet, H.-C. zur Loye, Advances in the synthesis and structural description of 2H-hexagonal perovskite-related oxides, Curr Opin Solid State Mater Sci. 5 (2001) 535–544. https://doi.org/10.1016/S1359-0286(01)00032-8.

[63] R. Mondal, H. Ratnawat, S. Mukherjee, A. Gupta, P. Singh, Investigation of the Role of Sr and Development of Superior Sr-Doped Hexagonal $BaCoO_{3-\delta}$ Perovskite Bifunctional OER/ORR Catalysts in Alkaline Media, Energy & Fuels. 36 (2022) 3219–3228. https://doi.org/10.1021/acs.energyfuels.2c00357.

[64] Q. Luo, D. Lin, W. Zhan, W. Zhang, L. Tang, J. Luo, Z. Gao, P. Jiang, M. Wang, L. Hao, K. Tang, Hexagonal Perovskite $Ba_{0.9}Sr_{0.1}Co_{0.8}Fe_{0.1}Ir_{0.1}O_{3-\delta}$ as an Efficient Electrocatalyst towards the Oxygen Evolution Reaction, ACS Appl Energy Mater. 3 (2020) 7149–7158. https://doi.org/10.1021/acsaem.0c01192.

[65] T. Erdil, E. Lokcu, I. Yildiz, C. Okuyucu, Y.E. Kalay, C. Toparli, Facile Synthesis and Origin of Enhanced Electrochemical Oxygen Evolution

Reaction Performance of 2H-Hexagonal $Ba_2CoMnO_{6-\delta}$ as a New Member in Double Perovskite Oxides, ACS Omega. 7 (2022) 44147–44155. https://doi.org/10.1021/acsomega.2c05627.

[66] H. Ruan, J.V. Barreras, T. Engstrom, Y. Merla, R. Millar, B. Wu, Lithium-ion battery lifetime extension: A review of derating methods, J Power Sources. 563 (2023) 232805. https://doi.org/10.1016/j.jpowsour.2023.232805.

[67] Y. Song, L. Wang, L. Sheng, D. Ren, H. Liang, Y. Li, A. Wang, H. Zhang, H. Xu, X. He, The significance of mitigating crosstalk in lithium-ion batteries: a review, Energy Environ Sci. 16 (2023) 1943–1963. https://doi.org/10.1039/D3EE00441D.

[68] B. Wang, E.H. Ang, Y. Yang, Y. Zhang, M. Ye, Q. Liu, C.C. Li, Post-Lithium-Ion Battery Era: Recent Advances in Rechargeable Potassium-Ion Batteries, Chemistry – A European Journal. 27 (2021) 512–536. https://doi.org/10.1002/chem.202001811.

[69] P. Keren Persis, R. Geetha, A Comparative Analysis on the Conventional Methods, Benefits of Recycling the Spent Lithium-ion Batteries with a Special focus on Ultrasonic Delamination., in: 2023 9th International Conference on Electrical Energy Systems (ICEES), IEEE, 2023: pp. 270–275. https://doi.org/10.1109/ICEES57979.2023.10110162.

[70] M. He, P. Zhang, X. Duan, L. Teng, H. Li, F. Meng, Q. Liu, W. Liu, Selective recovery of lithium from spent lithium-ion battery by an emission-free sulfation roasting strategy, Process Safety and Environmental Protection. (2023). https://doi.org/10.1016/j.psep.2023.07.065.

[71] Md.A. Rahman, X. Wang, C. Wen, High Energy Density Metal-Air Batteries: A Review, J Electrochem Soc. 160 (2013) A1759–A1771. https://doi.org/10.1149/2.062310jes.

[72] P. Pei, K. Wang, Z. Ma, Technologies for extending zinc–air battery's cyclelife: A review, Appl Energy. 128 (2014) 315–324. https://doi.org/10.1016/j.apenergy.2014.04.095.

[73] A. Bayaguud, Y. Fu, C. Zhu, Interfacial parasitic reactions of zinc anodes in zinc ion batteries: Underestimated corrosion and hydrogen evolution reactions and their suppression strategies, Journal of Energy Chemistry. 64 (2022) 246–262. https://doi.org/10.1016/j.jechem.2021.04.016.

[74] T.S. Lee, Hydrogen Over potential on Pure Metals in Alkaline Solution, J Electrochem Soc. 118 (1971) 1278. https://doi.org/10.1149/1.2408305.

[75] C.W. Lee, K. Sathiyanarayanan, S.W. Eom, M.S. Yun, Novel alloys to improve the electrochemical behavior of zinc anodes for zinc/air battery, J Power Sources. 160 (2006) 1436–1441. https://doi.org/10.1016/j.jpowsour.2006.02.019.

[76] L. Binder, K. Kordesch, Corrosion of zinc electrode mixtures in alkaline media, J Electroanal Chem Interfacial Electrochem. 180 (1984) 495–510. https://doi.org/10.1016/0368-1874(84)83603-5.

[77] T.I. Devyatkina, Yu.L. Gun'ko, M.G. Mikhalenko, Development of Ways To Diminish Corrosion of Zinc Electrode, Russian Journal of Applied Chemistry. 74 (2001) 1122–1125. https://doi.org/10.1023/A:1013058615990.

[78] M.V. Simičić, K.I. Popov, N.V. Krstajić, An experimental study of zinc morphology in alkaline electrolyte at low direct and pulsating overpotentials, Journal of Electroanalytical Chemistry. 484 (2000) 18–23. https://doi.org/10.1016/S0022-0728(00)00035-8.

[79] R.Y. Wang, D.W. Kirk, G.X. Zhang, Effects of Deposition Conditions on the Morphology of Zinc Deposits from Alkaline Zincate Solutions, J Electrochem Soc. 153 (2006) C357. https://doi.org/10.1149/1.2186037.

[80] K. Harting, U. Kunz, T. Turek, Zinc-air Batteries: Prospects and Challenges for Future Improvement, Zeitschrift Für Physikalische Chemie. 226 (2012) 151–166. https://doi.org/10.1524/zpch.2012.0152.

[81] K. Wang, P. Pei, Z. Ma, H. Chen, H. Xu, D. Chen, X. Wang, Dendrite growth in the recharging process of zinc–air batteries, J Mater Chem A Mater. 3 (2015) 22648–22655. https://doi.org/10.1039/C5TA06366C.

[82] Y. Shen, K. Kordesch, The mechanism of capacity fade of rechargeable alkaline manganese dioxide zinc cells, J Power Sources. 87 (2000) 162–166. https://doi.org/10.1016/S0378-7753(99)00476-0.

[83] K. Wang, P. Pei, Z. Ma, H. Xu, P. Li, X. Wang, Morphology control of zinc regeneration for zinc–air fuel cell and battery, J Power Sources. 271 (2014) 65–75. https://doi.org/10.1016/j.jpowsour.2014.07.182.

[84] C.-Y. Jung, T.-H. Kim, W.-J. Kim, S.-C. Yi, Computational analysis of the zinc utilization in the primary zinc-air batteries, Energy. 102 (2016) 694–704. https://doi.org/10.1016/j.energy.2016.02.084.

[85] R. GILLIAM, J. GRAYDON, D. KIRK, S. THORPE, A review of specific conductivities of potassium hydroxide solutions for various concentrations and temperatures, Int J Hydrogen Energy. 32 (2007) 359–364. https://doi.org/10.1016/j.ijhydene.2006.10.062.

[86] X.G. Zhang, Fibrous zinc anodes for high power batteries, J Power Sources. 163 (2006) 591–597. https://doi.org/10.1016/j.jpowsour.2006.09.034.

[87] B.A. Bouwhuis, J.L. McCrea, G. Palumbo, G.D. Hibbard, Mechanical properties of hybrid nanocrystalline metal foams, Acta Mater. 57 (2009) 4046–4053. https://doi.org/10.1016/j.actamat.2009.04.053.

[88] Z. Yan, E. Wang, L. Jiang, G. Sun, Superior cycling stability and high rate capability of three-dimensional Zn/Cu foam electrodes for zinc-based

alkaline batteries, RSC Adv. 5 (2015) 83781–83787. https://doi.org/10.1039/C5RA16264E.

[89] J.F. Parker, C.N. Chervin, E.S. Nelson, D.R. Rolison, J.W. Long, Wiring zinc in three dimensions re-writes battery performance—dendrite-free cycling, Energy Environ. Sci. 7 (2014) 1117–1124. https://doi.org/10.1039/C3EE43754J.

[90] J. Fu, D.U. Lee, F.M. Hassan, L. Yang, Z. Bai, M.G. Park, Z. Chen, Flexible High-Energy Polymer-Electrolyte-Based Rechargeable Zinc-Air Batteries, Advanced Materials. 27 (2015) 5617–5622. https://doi.org/10.1002/adma.201502853.

[91] P. Bonnick, J.R. Dahn, A Simple Coin Cell Design for Testing Rechargeable Zinc-Air or Alkaline Battery Systems, J Electrochem Soc. 159 (2012) A981–A989. https://doi.org/10.1149/2.023207jes.

[92] R. Wang, Z. Yang, B. Yang, T. Wang, Z. Chu, Superior cycle stability and high rate capability of Zn–Al–In-hydrotalcite as negative electrode materials for Ni–Zn secondary batteries, J Power Sources. 251 (2014) 344–350. https://doi.org/10.1016/j.jpowsour.2013.11.071.

[93] R.Y. Wang, D.W. Kirk, G.X. Zhang, Effects of Deposition Conditions on the Morphology of Zinc Deposits from Alkaline Zincate Solutions, J Electrochem Soc. 153 (2006) C357. https://doi.org/10.1149/1.2186037.

[94] R. Wang, Z. Yang, B. Yang, X. Fan, T. Wang, A novel alcohol-thermal synthesis method of calcium zincates negative electrode materials for Ni–Zn secondary batteries, J Power Sources. 246 (2014) 313–321. https://doi.org/10.1016/j.jpowsour.2013.07.097.

[95] H. Yang, H. Zhang, X. Wang, J. Wang, X. Meng, Z. Zhou, Calcium Zincate Synthesized by Ballmilling as a Negative Material for Secondary Alkaline Batteries, J Electrochem Soc. 151 (2004) A2126. https://doi.org/10.1149/1.1815158.

[96] J. Huang, Z. Yang, R. Wang, Z. Zhang, Z. Feng, X. Xie, Zn–Al layered double oxides as high-performance anode materials for zinc-based secondary battery, J Mater Chem A Mater. 3 (2015) 7429–7436. https://doi.org/10.1039/C5TA00279F.

[97] C. Mou, Y. Bai, C. Zhao, G. Wang, Y. Ren, Y. Liu, X. Wu, H. Wang, Y. Sun, Construction of a self-supported dendrite-free zinc anode for high-performance zinc–air batteries, Inorg Chem Front. 10 (2023) 3082–3090. https://doi.org/10.1039/D3QI00279A.

[98] L. Wang, X. Wang, B. Song, Z. Wang, F. Wan, Highly Reversible Zinc Anode Achieved by Surface Polyimide Coating for High-Performance Aqueous Zinc-Ion Batteries, Energy Technology. 11 (2023) 2201084. https://doi.org/10.1002/ente.202201084.

[99] R. Qin, Y. Wang, L. Yao, L. Yang, Q. Zhao, S. Ding, L. Liu, F. Pan, Progress in interface structure and modification of zinc anode for aqueous batteries, Nano Energy. 98 (2022) 107333. https://doi.org/10.1016/j.nanoen.2022.107333.

[100] J.-S. Lee, S. Tai Kim, R. Cao, N.-S. Choi, M. Liu, K.T. Lee, J. Cho, Metal-Air Batteries with High Energy Density: Li-Air versus Zn-Air, Adv Energy Mater. 1 (2011) 34–50. https://doi.org/10.1002/aenm.201000010.

[101] D.M. See, R.E. White, Temperature and Concentration Dependence of the Specific Conductivity of Concentrated Solutions of Potassium Hydroxide, J Chem Eng Data. 42 (1997) 1266–1268. https://doi.org/10.1021/je970140x.

[102] P.C. Ho, D.A. Palmer, R.H. Wood, Conductivity Measurements of Dilute Aqueous LiOH, NaOH, and KOH Solutions to High Temperatures and Pressures Using a Flow-Through Cell, J Phys Chem B. 104 (2000) 12084–12089. https://doi.org/10.1021/jp000845x.

[103] J.-F. Drillet, F. Holzer, T. Kallis, S. Müller, V.M. Schmidt, Influence of CO2 on the stability of bifunctional oxygen electrodes for rechargeable

zinc/air batteries and study of different CO2 filter materials, Physical Chemistry Chemical Physics. 3 (2001) 368–371. https://doi.org/10.1039/b005523i.

[104] H.-H. Cheng, C.-S. Tan, Reduction of CO2 concentration in a zinc/air battery by absorption in a rotating packed bed, J Power Sources. 162 (2006) 1431–1436. https://doi.org/10.1016/j.jpowsour.2006.07.046.

[105] Z. Ma, P. Pei, K. Wang, X. Wang, H. Xu, Y. Liu, G. peng, Degradation characteristics of air cathode in zinc air fuel cells, J Power Sources. 274 (2015) 56–64. https://doi.org/10.1016/j.jpowsour.2014.10.030.

[106] J. Fu, D.U. Lee, F.M. Hassan, L. Yang, Z. Bai, M.G. Park, Z. Chen, Flexible High-Energy Polymer-Electrolyte-Based Rechargeable Zinc-Air Batteries, Advanced Materials. 27 (2015) 5617–5622. https://doi.org/10.1002/adma.201502853.

[107] J. Fu, J. Zhang, X. Song, H. Zarrin, X. Tian, J. Qiao, L. Rasen, K. Li, Z. Chen, A flexible solid-state electrolyte for wide-scale integration of rechargeable zinc–air batteries, Energy Environ Sci. 9 (2016) 663–670. https://doi.org/10.1039/C5EE03404C.

[108] J. Fu, F.M. Hassan, J. Li, D.U. Lee, A.R. Ghannoum, G. Lui, Md.A. Hoque, Z. Chen, Flexible Rechargeable Zinc-Air Batteries through Morphological Emulation of Human Hair Array, Advanced Materials. 28 (2016) 6421–6428. https://doi.org/10.1002/adma.201600762.

[109] D.U. Lee, J.-Y. Choi, K. Feng, H.W. Park, Z. Chen, Advanced Extremely Durable 3D Bifunctional Air Electrodes for Rechargeable Zinc-Air Batteries, Adv Energy Mater. 4 (2014) 1301389. https://doi.org/10.1002/aenm.201301389.

[110] Y. Wang, W.-H. Zhong, Development of Electrolytes towards Achieving Safe and High-Performance Energy-Storage Devices: A Review,

ChemElectroChem. 2 (2015) 22–36. https://doi.org/10.1002/celc.201402277.

[111] Y.-J. Wang, J. Qiao, R. Baker, J. Zhang, Alkaline polymer electrolyte membranes for fuel cell applications, Chem Soc Rev. 42 (2013) 5768. https://doi.org/10.1039/c3cs60053j.

[112] M. Huynh, C. Shi, S.J.L. Billinge, D.G. Nocera, Nature of Activated Manganese Oxide for Oxygen Evolution, J Am Chem Soc. 137 (2015) 14887–14904. https://doi.org/10.1021/jacs.5b06382.

[113] C.C.L. McCrory, S. Jung, J.C. Peters, T.F. Jaramillo, Benchmarking Heterogeneous Electrocatalysts for the Oxygen Evolution Reaction, J Am Chem Soc. 135 (2013) 16977–16987. https://doi.org/10.1021/ja407115p.

[114] I. Katsounaros, S. Cherevko, A.R. Zeradjanin, K.J.J. Mayrhofer, Oxygen Electrochemistry as a Cornerstone for Sustainable Energy Conversion, Angewandte Chemie International Edition. 53 (2014) 102–121. https://doi.org/10.1002/anie.201306588.

[115] T.X. Nguyen, Y. Liao, C. Lin, Y. Su, J. Ting, Advanced High Entropy Perovskite Oxide Electrocatalyst for Oxygen Evolution Reaction, Adv Funct Mater. 31 (2021) 2101632. https://doi.org/10.1002/adfm.202101632.

[116] Y. Bu, O. Gwon, G. Nam, H. Jang, S. Kim, Q. Zhong, J. Cho, G. Kim, A Highly Efficient and Robust Cation Ordered Perovskite Oxide as a Bifunctional Catalyst for Rechargeable Zinc-Air Batteries, ACS Nano. 11 (2017) 11594–11601. https://doi.org/10.1021/acsnano.7b06595.

[117] S.B. Park, Y. Park, Fabrication of gas diffusion layer (GDL) containing microporous layer using flourinated ethylene prophylene (FEP) for proton exchange membrane fuel cell (PEMFC), International Journal of Precision Engineering and Manufacturing. 13 (2012) 1145–1151. https://doi.org/10.1007/s12541-012-0152-x.

[118] S. Suren, S. Kheawhom, Development of a High Energy Density Flexible Zinc-Air Battery, J Electrochem Soc. 163 (2016) A846–A850. https://doi.org/10.1149/2.0361606jes.

[119] E. Davari, A.D. Johnson, A. Mittal, M. Xiong, D.G. Ivey, Manganese-cobalt mixed oxide film as a bifunctional catalyst for rechargeable zinc-air batteries, Electrochim Acta. 211 (2016) 735–743. https://doi.org/10.1016/j.electacta.2016.06.085.

[120] S. Guo, S. Zhang, S. Sun, Tuning Nanoparticle Catalysis for the Oxygen Reduction Reaction, Angewandte Chemie International Edition. 52 (2013) 8526–8544. https://doi.org/10.1002/anie.201207186.

[121] X. Xu, Y. Zhong, Z. Shao, Double Perovskites in Catalysis, Electrocatalysis, and Photo(electro)catalysis, Trends Chem. 1 (2019) 410–424. https://doi.org/10.1016/j.trechm.2019.05.006.

[122] N.-I. Kim, Y.J. Sa, T.S. Yoo, S.R. Choi, R.A. Afzal, T. Choi, Y.-S. Seo, K.-S. Lee, J.Y. Hwang, W.S. Choi, S.H. Joo, J.-Y. Park, Oxygen-deficient triple perovskites as highly active and durable bifunctional electrocatalysts for oxygen electrode reactions, Sci Adv. 4 (2018). https://doi.org/10.1126/sciadv.aap9360.

[123] J. Wang, Y. Gao, D. Chen, J. Liu, Z. Zhang, Z. Shao, F. Ciucci, Water Splitting with an Enhanced Bifunctional Double Perovskite, ACS Catal. 8 (2018) 364–371. https://doi.org/10.1021/acscatal.7b02650.

[124] C.-F. Chen, G. King, R.M. Dickerson, P.A. Papin, S. Gupta, W.R. Kellogg, G. Wu, Oxygen-deficient BaTiO3− perovskite as an efficient bifunctional oxygen electrocatalyst, Nano Energy. 13 (2015) 423–432. https://doi.org/10.1016/j.nanoen.2015.03.005.

[125] Y. Du, S. Khan, X. Zhang, G. Yu, R. Liu, B. Zheng, R. Nadimicherla, D. Wu, R. Fu, In-situ preparation of porous carbon nanosheets loaded with

metal chalcogenides for a superior oxygen evolution reaction, Carbon N Y. 149 (2019) 144–151. https://doi.org/10.1016/j.carbon.2019.04.048.

[126] G. Janani, S. Yuvaraj, S. Surendran, Y. Chae, Y. Sim, S.-J. Song, W. Park, M.-J. Kim, U. Sim, Enhanced bifunctional electrocatalytic activity of Ni-Co bimetallic chalcogenides for efficient water-splitting application, J Alloys Compd. 846 (2020) 156389. https://doi.org/10.1016/j.jallcom.2020.156389.

[127] L. Ge, H. Yuan, Y. Min, L. Li, S. Chen, L. Xu, W.A. Goddard, Predicted Optimal Bifunctional Electrocatalysts for the Hydrogen Evolution Reaction and the Oxygen Evolution Reaction Using Chalcogenide Heterostructures Based on Machine Learning Analysis of in Silico Quantum Mechanics Based High Throughput Screening, J Phys Chem Lett. 11 (2020) 869–876. https://doi.org/10.1021/acs.jpclett.9b03875.

[128] A.P. Tiwari, D. Kim, Y. Kim, H. Lee, Bifunctional Oxygen Electrocatalysis through Chemical Bonding of Transition Metal Chalcogenides on Conductive Carbons, Adv Energy Mater. 7 (2017) 1602217. https://doi.org/10.1002/aenm.201602217.

[129] S. Jin, Are Metal Chalcogenides, Nitrides, and Phosphides Oxygen Evolution Catalysts or Bifunctional Catalysts?, ACS Energy Lett. 2 (2017) 1937–1938. https://doi.org/10.1021/acsenergylett.7b00679.

[130] S.S. Shinde, J.-Y. Yu, J.-W. Song, Y.-H. Nam, D.-H. Kim, J.-H. Lee, Highly active and durable carbon nitride fibers as metal-free bifunctional oxygen electrodes for flexible Zn–air batteries, Nanoscale Horiz. 2 (2017) 333–341. https://doi.org/10.1039/C7NH00058H.

[131] Y. Guan, G. Liu, J. Li, Y. Wang, Z. Zhang, Surface-engineered cobalt nitride composite as efficient bifunctional oxygen electrocatalyst, Nanotechnology. 30 (2019) 495406. https://doi.org/10.1088/1361-6528/ab4144.

[132] S.S. Shinde, C.-H. Lee, A. Sami, D.-H. Kim, S.-U. Lee, J.-H. Lee, Scalable 3-D Carbon Nitride Sponge as an Efficient Metal-Free Bifunctional Oxygen Electrocatalyst for Rechargeable Zn–Air Batteries, ACS Nano. 11 (2017) 347–357. https://doi.org/10.1021/acsnano.6b05914.

[133] S. Chen, X. Liu, H. Sun, Z. Cao, J. Xiong, Y. Li, Facile synthesis of carbon coated cobalt-cobalt molybdenum carbide as advanced bifunctional oxygen electrocatalyst for rechargeable Zn-air battery, J Alloys Compd. 897 (2022) 163203. https://doi.org/10.1016/j.jallcom.2021.163203.

[134] Y. Li, Z. Yin, M. Cui, S. Chen, T. Ma, Bimetallic cobalt molybdenum carbide–cobalt composites as superior bifunctional oxygen electrocatalysts for Zn–air batteries, Mater Today Energy. 18 (2020) 100565. https://doi.org/10.1016/j.mtener.2020.100565.

[135] H. Jiang, Y. Yao, Y. Zhu, Y. Liu, Y. Su, X. Yang, C. Li, Iron Carbide Nanoparticles Encapsulated in Mesoporous Fe–N-Doped Graphene-Like Carbon Hybrids as Efficient Bifunctional Oxygen Electrocatalysts, ACS Appl Mater Interfaces. 7 (2015) 21511–21520. https://doi.org/10.1021/acsami.5b06708.

[136] S. Liu, L. Xiao, G. Wang, G. Liu, Y. Mo, W. Lu, Heteroatom-doped carbon materials from bimetal covalent organic polymers as efficient bifunctional electrocatalysts in oxygen reduction and oxygen evolution reactions, Materials Today Sustainability. 22 (2023) 100389. https://doi.org/10.1016/j.mtsust.2023.100389.

[137] X. Li, T. Zhou, Z. Luo, L. Zhang, Z. Ren, Q. Zhang, C. He, X. Jiang, Y. Li, X. Ren, N, S heteroatom co-doped carbon-based materials carrying Mn and Co atoms as bifunctional catalysts for stable rechargeable zinc-air batteries, J Alloys Compd. 939 (2023) 168756. https://doi.org/10.1016/j.jallcom.2023.168756.

[138] L. Zong, P. Li, F. Lu, C. Wang, K. Fan, Z. Li, L. Wang, Assembling Amorphous Metal–Organic Frameworks onto Heteroatom-Doped Carbon Spheres for Remarkable Bifunctional Oxygen Electrocatalysis, Adv Funct Mater. 33 (2023). https://doi.org/10.1002/adfm.202301013.

[139] Y. Li, Q. Li, H. Wang, L. Zhang, D.P. Wilkinson, J. Zhang, Recent Progresses in Oxygen Reduction Reaction Electrocatalysts for Electrochemical Energy Applications, Electrochemical Energy Reviews. 2 (2019) 518–538. https://doi.org/10.1007/s41918-019-00052-4.

[140] M. Risch, Perovskite Electrocatalysts for the Oxygen Reduction Reaction in Alkaline Media, Catalysts. 7 (2017) 154. https://doi.org/10.3390/catal7050154.

[141] J. Suntivich, H.A. Gasteiger, N. Yabuuchi, H. Nakanishi, J.B. Goodenough, Y. Shao-Horn, Design principles for oxygen-reduction activity on perovskite oxide catalysts for fuel cells and metal–air batteries, Nat Chem. 3 (2011) 546–550. https://doi.org/10.1038/nchem.1069.

[142] S.H. Chang, J.G. Connell, N. Danilovic, R. Subbaraman, K.-C. Chang, V.R. Stamenkovic, N.M. Markovic, Activity–stability relationship in the surface electrochemistry of the oxygen evolution reaction, Faraday Discuss. 176 (2014) 125–133. https://doi.org/10.1039/C4FD00134F.

[143] Y. Liu, D. Zhou, T. Deng, G. He, A. Chen, X. Sun, Y. Yang, P. Miao, Research Progress of Oxygen Evolution Reaction Catalysts for Electrochemical Water Splitting, ChemSusChem. 14 (2021) 5359–5383. https://doi.org/10.1002/cssc.202101898.

[144] D. Guan, J. Zhou, Y.-C. Huang, C.-L. Dong, J.-Q. Wang, W. Zhou, Z. Shao, Screening highly active perovskites for hydrogen-evolving reaction via unifying ionic electronegativity descriptor, Nat Commun. 10 (2019) 3755. https://doi.org/10.1038/s41467-019-11847-w.

[145] X. Cheng, E. Fabbri, Y. Yamashita, I.E. Castelli, B. Kim, M. Uchida, R. Haumont, I. Puente-Orench, T.J. Schmidt, Oxygen Evolution Reaction on Perovskites: A Multieffect Descriptor Study Combining Experimental and Theoretical Methods, ACS Catal. 8 (2018) 9567–9578. https://doi.org/10.1021/acscatal.8b02022.

[146] C. Nicollet, C. Toparli, G.F. Harrington, T. Defferriere, B. Yildiz, H.L. Tuller, Acidity of surface-infiltrated binary oxides as a sensitive descriptor of oxygen exchange kinetics in mixed conducting oxides, Nat Catal. 3 (2020) 913–920. https://doi.org/10.1038/s41929-020-00520-x.

[147] L. Yang, G. Yu, X. Ai, W. Yan, H. Duan, W. Chen, X. Li, T. Wang, C. Zhang, X. Huang, J.-S. Chen, X. Zou, Efficient oxygen evolution electrocatalysis in acid by a perovskite with face-sharing IrO6 octahedral dimers, Nat Commun. 9 (2018) 5236. https://doi.org/10.1038/s41467-018-07678-w.

[148] J. Qiao, Different MnO_2 Nanotube As Bi-Functional Cathode Catalysts for Rechargeable Zinc-Air Batteries, ECS Meeting Abstracts. MA2016-01 (2016) 181–181. https://doi.org/10.1149/MA2016-01/1/181.

[149] B. Seo, Y.J. Sa, J. Woo, K. Kwon, J. Park, T.J. Shin, H.Y. Jeong, S.H. Joo, Size-Dependent Activity Trends Combined with in Situ X-ray Absorption Spectroscopy Reveal Insights into Cobalt Oxide/Carbon Nanotube-Catalyzed Bifunctional Oxygen Electrocatalysis, ACS Catal. 6 (2016) 4347–4355. https://doi.org/10.1021/acscatal.6b00553.

[150] I. Katsounaros, W.B. Schneider, J.C. Meier, U. Benedikt, P.U. Biedermann, A.A. Auer, K.J.J. Mayrhofer, Hydrogen peroxide electrochemistry on platinum: towards understanding the oxygen reduction reaction mechanism, Physical Chemistry Chemical Physics. 14 (2012) 7384. https://doi.org/10.1039/c2cp40616k.

[151] M. Shao, P. Liu, R.R. Adzic, Superoxide Anion is the Intermediate in the Oxygen Reduction Reaction on Platinum Electrodes, J Am Chem Soc. 128 (2006) 7408–7409. https://doi.org/10.1021/ja061246s.

[152] I. Katsounaros, W.B. Schneider, J.C. Meier, U. Benedikt, P.U. Biedermann, A. Cuesta, A.A. Auer, K.J.J. Mayrhofer, The impact of spectator species on the interaction of H2O2 with platinum – implications for the oxygen reduction reaction pathways, Physical Chemistry Chemical Physics. 15 (2013) 8058. https://doi.org/10.1039/c3cp50649e.

[153] U.I. Kramm, J. Herranz, N. Larouche, T.M. Arruda, M. Lefèvre, F. Jaouen, P. Bogdanoff, S. Fiechter, I. Abs-Wurmbach, S. Mukerjee, J.-P. Dodelet, Structure of the catalytic sites in Fe/N/C-catalysts for O2-reduction in PEM fuel cells, Physical Chemistry Chemical Physics. 14 (2012) 11673. https://doi.org/10.1039/c2cp41957b.

[154] F. Jaouen, E. Proietti, M. Lefèvre, R. Chenitz, J.-P. Dodelet, G. Wu, H.T. Chung, C.M. Johnston, P. Zelenay, Recent advances in non-precious metal catalysis for oxygen-reduction reaction in polymer electrolyte fuelcells, Energy Environ. Sci. 4 (2011) 114–130. https://doi.org/10.1039/C0EE00011F.

[155] Z. Chen, D. Higgins, A. Yu, L. Zhang, J. Zhang, A review on non-precious metal electrocatalysts for PEM fuel cells, Energy Environ Sci. 4 (2011) 3167. https://doi.org/10.1039/c0ee00558d.

[156] X. Ren, Q. Lv, L. Liu, B. Liu, Y. Wang, A. Liu, G. Wu, Current progress of Pt and Pt-based electrocatalysts used for fuel cells, Sustain Energy Fuels. 4 (2020) 15–30. https://doi.org/10.1039/C9SE00460B.

[157] M.R. Tarasevich, O. V. Korchagin, Electrocatalysis and pH (a review), Russian Journal of Electrochemistry. 49 (2013) 600–618. https://doi.org/10.1134/S102319351307015X.

[158] N. Danilovic, R. Subbaraman, K.-C. Chang, S.H. Chang, Y.J. Kang, J. Snyder, A.P. Paulikas, D. Strmcnik, Y.-T. Kim, D. Myers, V.R. Stamenkovic, N.M. Markovic, Activity–Stability Trends for the Oxygen Evolution Reaction on Monometallic Oxides in Acidic Environments, J Phys Chem Lett. 5 (2014) 2474–2478. https://doi.org/10.1021/jz501061n.

[159] A. Grimaud, K.J. May, C.E. Carlton, Y.-L. Lee, M. Risch, W.T. Hong, J. Zhou, Y. Shao-Horn, Double perovskites as a family of highly active catalysts for oxygen evolution in alkaline solution, Nat Commun. 4 (2013) 2439. https://doi.org/10.1038/ncomms3439.

[160] C. Bloed, J. Vuong, A. Enriquez, S. Raghavan, I. Tran, S. Derakhshan, H. Tavassol, Oxygen Vacancy and Chemical Ordering Control Oxygen Evolution Activity of $Sr_{2-x}Ca_xFe_2O_{6-\delta}$ Perovskites, ACS Appl Energy Mater. 2 (2019) 6140–6145. https://doi.org/10.1021/acsaem.9b00581.

[161] R. Søndenå, S. Stølen, P. Ravindran, T. Grande, N.L. Allan, Corner- versus face-sharing octahedra in AMnO3 perovskites (A = Ca, Sr, and Ba), Phys Rev B. 75 (2007) 184105. https://doi.org/10.1103/PhysRevB.75.184105.

[162] E. Lökçü, Ç. Toparli, M. Anik, Electrochemical Performance of $(MgCoNiZn)_{1-x}Li_xO$ High-Entropy Oxides in Lithium-Ion Batteries, ACS Appl Mater Interfaces. 12 (2020) 23860–23866. https://doi.org/10.1021/acsami.0c03562.

[163] M. Huynh, D.K. Bediako, D.G. Nocera, A Functionally Stable Manganese Oxide Oxygen Evolution Catalyst in Acid, J Am Chem Soc. 136 (2014) 6002–6010. https://doi.org/10.1021/ja413147e.